

Lightlike Geodesics and Gravitational Lensing in the Spacetime of an Accelerating Black Hole

Torben C Frost and Volker Perlick

ZARM, University of Bremen, 28359 Bremen, Germany.

Email: torben.frost@zarm.uni-bremen.de, volker.perlick@zarm.uni-bremen.de

January 20, 2021

Abstract. The C-metric is a solution to Einstein's vacuum field equation that describes an accelerating black hole. In this paper we discuss the propagation of light rays and the resulting lensing features in this metric. We first solve the lightlike geodesic equation using elliptic integrals and Jacobi elliptic functions. Then we fix a static observer in the region of outer communication of the C-metric and introduce an orthonormal tetrad to parameterise the directions of the light rays ending at the position of the observer using latitude-longitude coordinates on the observer's celestial sphere. In this parameterisation we rederive the angular radius of the shadow, we formulate a lens equation, and we derive the redshift and the travel time of light rays. We discuss the relevance of our theoretical results for detecting accelerating black holes described by the C-metric and for distinguishing them from non-accelerating black holes.

1. Introduction

In 2019 the Event Horizon Telescope (EHT) Collaboration released images showing the shadow of the supermassive black hole in the core of the galaxy M87 observed in April 2017 [1]. Besides being a significant scientific achievement in itself this observation also provided an additional confirmation of general relativity: The observed features were found to be in agreement with the assumption that at the centre of M87 there is a Kerr black hole.

Currently the resolution of the EHT is limited by the distribution of radio telescopes on Earth and thus extension of Very Long Baseline Interferometry (VLBI) to space is needed for further increasing its resolution. Space VLBI has a tradition since the late 1970s and made particular progress with the Spektr-R satellite that was part of the RadioAstron programme [2, 3] and terminated operation in 2019. However, for the EHT one needs radio telescopes that can operate at millimeter or submillimeter wavelengths. Space VLBI with telescopes in this range has not been done so far, but projects that are attempting to do this are now at the planning stage. When realised, this will allow us observing the shadow and other lensing features of supermassive black holes with unprecedented accuracy. In particular, it will then be possible to use this kind of observations for discriminating between different black hole models. On the basis of general relativity, the Kerr metric or, in the case of vanishing rotation, the Schwarzschild metric is the standard model for an uncharged black hole. However, Einstein's vacuum field equation admits more general black hole solutions. Their astrophysical relevance is unclear because they are exotic in the sense that the spacetime outside of the horizon is either not free of singularities or not asymptotically flat (or both). Future observations could make it possible to distinguish Kerr black holes from these exotic black holes by their lensing features. For this reason, it is of relevance to theoretically study the lensing features of exotic black holes. Moreover, such investigations are of some interest by itself because they illustrate what kind of mathematical peculiarities are allowed by the vacuum field equation.

In this paper we want to discuss the lensing features of one of these exotic solutions which is known as the C-metric. It was found already in 1918 by Levi-Civita [4] and belongs to the family of Plebański-Demiański electrovacuum spacetimes with cosmological constant [5]. The name C-metric refers to a review by Ehlers and Kundt [6] who rediscovered this metric within three classes of vacuum solutions they labelled A, B and C. The C-metric is discussed in detail in an article by Griffiths et al. [7] and in a book by Griffiths and Podolský [8]. As outlined in these works, the C-metric describes an accelerating black hole. (The maximal analytical extension actually describes two black holes accelerating in opposite directions; however, as these two black holes live in causally disconnected regions, it is reasonable to restrict the consideration to one of them.) The metric depends on two parameters, a mass parameter m and an acceleration parameter α . For $\alpha = 0$ it reduces to the Schwarzschild metric. This is in agreement with the fact that for a black hole in uniform motion the metric of the ambient spacetime can be

reduced to the Schwarzschild metric by a Lorentz transformation. Note, however, that this Lorentz transformation becomes singular if the velocity of the black hole approaches the speed of light, see Aichelburg and Sexl [9].

In the C-metric the acceleration of the black hole is caused either by a string that pulls the black hole or by a strut that pushes it (or by both). The string and the strut manifest themselves as conical singularities; one of them, but not both, could be removed by changing the periodicity of the φ coordinate, as was first observed by Kinnersley and Walker [10], cf. Griffiths and Podolský [8]. Recently Kofroň [11] interpreted the string and the strut as a null dust. He associated the asymmetry of the C-metric with a momentum flux towards the black hole through the strut and away from the black hole through the string. While one can hardly expect a black hole with such a string or a strut attached to be literally realised in Nature, there might be accelerating black holes that can be described by such a model to within a reasonable approximation. In any case, history has taught us that solutions to Einstein's vacuum field equation should be taken seriously.

Whereas the topological and causal structure of the C-metric has been investigated by many authors, the geodesics in this metric have been studied only partially. Farhoosh and Zimmerman [12] investigated the motion on radial timelike geodesics. In 2001 Pravda and Pravdova [13] analytically derived relations for describing the circular motion of massive and massless particles (photons) about the axis. In the same year Chamblin [14] qualitatively extended their analysis to circular motion in the C-metric with a negative cosmological constant. Both studies came to the conclusion that circular null geodesics are unstable. Podolský et al. [15] discussed several special features of the null geodesic equation in the C-metric with a negative cosmological constant; however, they provided an explicit exact solution only for geodesics with, in their notation, $J = Q = 0$. Bini et al. [16] investigated the motion of spinning particles on circular geodesics about the axis with the C-metric as background. The most detailed study of timelike and null geodesics in the C-metric was provided by Lim [17] who used a combination of analytical and numerical methods. However, his study mainly focused on timelike geodesics and provided explicit analytic solutions only for the radius coordinate on the axes and the time coordinate of radial null geodesics.

Of particular interest in the C-metric is the photon sphere, which is filled with unstable null geodesics. Its existence gives rise to the shadow of a black hole that can be observed by VLBI. Grenzebach et al. [18, 19] determined in Boyer-Lindquist-like coordinates the shadow of an accelerating black hole with additional spin and NUT parameter. Specifying their equations (22), (27a) and (29) to the case of vanishing spin and vanishing NUT parameter gives the photon sphere and the angular radius of the shadow in the C-metric. In Hong-Teo coordinates [20] the photon sphere in the C-metric was investigated by Gibbons and Warnick [21]. In particular, they showed that its intrinsic geometry is not that of a “round sphere” (i.e., of a sphere isometrically embedded into Euclidean 3-space) but that it has at least one conical singularity. They also plotted parts of a geodesic on that surface; however, they did not explicitly

discuss analytic solutions to the equations of motion. Recently Alrais Alawadi et al. [22] rederived, in Boyer-Lindquist-like coordinates, the coordinate radius of the photon sphere and they also determined the coordinate angle of what we will refer to as the photon cone. In addition they performed a stability analysis and found that the circular null geodesic at the intersection of the photon sphere and the photon cone is unstable with respect to radial perturbations. Actually, all lightlike geodesics in the photon sphere are unstable with respect to radial perturbations as will be discussed below.

So it is fair to say that a comprehensive presentation of analytical solutions to the lightlike geodesic equation in the C-metric is not yet available in the literature. It is one of the main goals of this paper to provide such a presentation. Such analytical solutions have the benefit of clearly showing the influence of each parameter onto the geodesics. This is a major advantage over numerical solutions. Moreover, it was argued by several authors, e.g. by Yang and Wang [23] who considered light rays in the Kerr spacetime, that an analytical representation of the geodesics is useful also for ray-tracing codes because it reduces the computation time.

Therefore the first objective of this paper is to analytically solve the equations of motion for lightlike geodesics in the C-metric. We approach this problem by using Jacobi's elliptic functions and Legendre's elliptic integrals. For the Schwarzschild spacetime, this approach has a very long tradition, beginning in 1920 with a short paper by Forsyth [24] and a detailed investigation by Morton [25]. Jacobi's elliptic functions were also used in 1959 by Darwin [26] who discussed important features of lightlike and timelike geodesics in the Schwarzschild metric and, much more recently, for lightlike geodesics in the Kerr metric by Yang and Wang [23] and by Gralla and Lupsasca [27].

The analytical solutions of the lightlike geodesic equation in the C-metric will allow us to study, in the second part of the paper, the relevant lensing features of an accelerating black hole. We will calculate the angular radius of the shadow, we will set up a lens equation, and we will discuss the redshift and the travel time of light in the C-metric. Up to now there are only partial results in this direction available in the literature. We have already mentioned that Grenzebach et al. [18, 19] discussed the shadow in a class of spacetimes that contains the C-metric as a special case. Sharif and Iftikhar [28] considered the bending angle of light rays in the equatorial plane of the C-metric with additional spin and NUT parameter. This analysis does not apply to the case of the pure C-metric (without spin and without NUT parameter) because in this case the only lightlike geodesics in the equatorial plane are the radial ones, as will become clear later in this paper. Alrais Alawadi et al. [22] calculated the bending angle of light rays on the photon cone, however, since the angle of the photon cone is unique for any chosen value of the acceleration parameter α this calculation only considers a very limited set of null geodesics.

The remainder of the paper is structured as follows. In Section 2 we summarise, for the reader's convenience, the main properties of the C-metric. In Section 3 we discuss and solve the equations of motion for lightlike geodesics. In Section 4 we discuss the

main lensing features in the C-metric, i.e., the angular radius of the shadow, the lens equation, the redshift and the travel time of light. In addition we address the question of how the influence of the acceleration parameter can actually be measured.

Throughout the paper we use geometrical units such that $c = G = 1$. The convention for the metric signature is $(-, +, +, +)$.

2. The C-metric

The C-metric depends on two parameters, a mass parameter m with the dimension of a length and an acceleration parameter α with the dimension of an inverse length. For $\alpha = 0$ it reduces to the Schwarzschild metric. In Boyer-Lindquist-like coordinates the metric reads [7, 8]

$$g_{\mu\nu}(x)dx^\mu dx^\nu = \frac{1}{\Omega(r, \vartheta)^2} \left(-Q(r)dt^2 + \frac{dr^2}{Q(r)} + \frac{r^2 d\vartheta^2}{P(\vartheta)} + r^2 P(\vartheta) \sin^2 \vartheta d\varphi^2 \right), \quad (1)$$

where

$$\Omega(r, \vartheta) = 1 - \alpha r \cos \vartheta, \quad (2)$$

$$Q(r) = \left(1 - \alpha^2 r^2\right) \left(1 - \frac{2m}{r}\right), \quad (3)$$

$$P(\vartheta) = 1 - 2\alpha m \cos \vartheta. \quad (4)$$

Throughout this article, we follow the convention in [8]. We assume $m > 0$ and $\alpha > 0$, treating the case $\alpha = 0$ as a limit. Excluding negative values of α is no restriction of generality because the C-metric with $-\alpha$ is isometric to the C-metric with α , where the isometry is given by the reflection at the equatorial plane, $\vartheta \mapsto \pi - \vartheta$. Note, however, that some authors, e.g. Griffiths et al. [7], call α what we call $-\alpha$.

The C-metric is static and axisymmetric and thus has two Killing vector fields $K_t = \partial_t$ and $K_\varphi = \partial_\varphi$. The vector field $K_t = \partial_t$ is associated with the invariance of the metric under time translations and generates a boost symmetry. The vector field $K_\varphi = \partial_\varphi$ is associated with the invariance of the metric under rotations about the axis of symmetry $\sin \vartheta = 0$. As already mentioned in the Introduction, the C-metric is usually interpreted as describing an accelerating black hole; the justification for this interpretation is discussed in detail in the book by Griffiths and Podolský [8]. Observers on t -lines move with the black hole in such a way that they see a time-independent metric.

The t coordinate ranges over all of \mathbb{R} and the angle coordinates ϑ and φ are assumed to have their usual range as standard coordinates on the 2-sphere; in particular, φ is assumed to be 2π -periodic. Then there is a conical singularity on the axis $\sin \vartheta = 0$, i.e., the condition of elementary flatness is violated. For $\alpha > 0$ a plane that crosses the half-axis $\vartheta = 0$ has a deficit angle and a plane that crosses the half-axis $\vartheta = \pi$ has a surplus angle. This may be interpreted as saying that at $\vartheta = 0$ there is a string (with a tension, that pulls the black hole) and that at $\vartheta = \pi$ there is a strut (with a pressure,

that pushes the black hole), see e.g. Griffiths et al. [7, 8]. By giving the φ coordinate a periodicity different from 2π one could remove the conical singularity on one of the two half-axes, but not on both. Several authors, e.g. Griffiths and Podolský [8], advocate the idea of removing the conical singularity at $\vartheta = \pi$. We will not do this here, so that the reader can see the effect both of the string and of the strut. In view of the range of the angular coordinates it is also important to note that $P(\vartheta)$ must be positive. If $2m\alpha > 1$, this bounds the ϑ coordinate away from the axis $\sin \vartheta = 0$ which seems to be unphysical. Therefore, we will soon restrict α to values such that $2m\alpha < 1$.

For discussing the range of the r coordinate we have to investigate at which r -values the metric, in the Boyer-Lindquist-like coordinates, becomes singular. This is the case if $r = 0$, $\Omega(r, \vartheta) = 0$, or $Q(r) = 0$. Analogously to the Schwarzschild metric, the C-metric has a curvature singularity at $r = 0$, limiting the motion of particles and light rays to the domain $r > 0$. The conformal factor $\Omega(r, \vartheta)$ vanishes when [7]

$$r = \frac{1}{\alpha \cos \vartheta} \quad (5)$$

which is possible, as $r > 0$, only if $0 \leq \vartheta < \frac{\pi}{2}$. This singularity corresponds to conformal infinity. It starts at $r = 1/\alpha$ for $\vartheta = 0$ and stretches out to $r = \infty$ for $\vartheta = \frac{\pi}{2}$. For $\frac{\pi}{2} \leq \vartheta \leq \pi$ the r coordinate extends to infinity. The function $Q(r)$ vanishes at $r_{BH} = 2m$ and at $r_\alpha = \frac{1}{\alpha}$. Both are coordinate singularities which can be removed using appropriate coordinate transformations (see, e.g., Griffiths et al. [7]). These coordinate singularities lead to the existence of horizons. Here we have to distinguish three different cases. Figure 1 shows the horizon structure for the three cases and for the Schwarzschild metric. Note that the angular coordinates are suppressed and that, correspondingly, the singularities at $\Omega(r, \vartheta) = 0$, $\sin \vartheta = 0$ and (possibly) $P(\vartheta) = 0$ are not shown.

In case one (figure 1b) we have $r_{BH} < r_\alpha$. In this case the coordinate singularity at r_{BH} marks the position of the black hole horizon while the second coordinate singularity marks the position of an outer horizon. Because the existence of the outer horizon arises from a non-vanishing α it is usually referred to as the acceleration horizon. In the region between the two horizons ∂_t is timelike while ∂_r is spacelike. Thus this region is static. In the other two regions the causal character of ∂_t and ∂_r is reversed, so these regions are non-static. – In the second case (figure 1c) we have $r_{BH} = r_\alpha$. Here we have a degenerate horizon separating two non-static regions. – In the last case (figure 1d) we have $r_\alpha < r_{BH}$, i.e., the acceleration horizon becomes the inner horizon. This is the case where the ϑ coordinate is restricted by the condition $P(\vartheta) > 0$. We have already mentioned that this case is usually considered unphysical. Therefore, from now on we assume that

$$0 < m, \quad 0 < \alpha < \frac{1}{2m}. \quad (6)$$

In this paper we are interested in lensing, assuming that both the light sources and the observers are in the domain of outer communication, i.e. in region 2 of figure 1b. Note that a light ray (or any other signal) that has left this domain can never re-enter. Therefore we need to consider only null geodesics in the domain of outer communication.

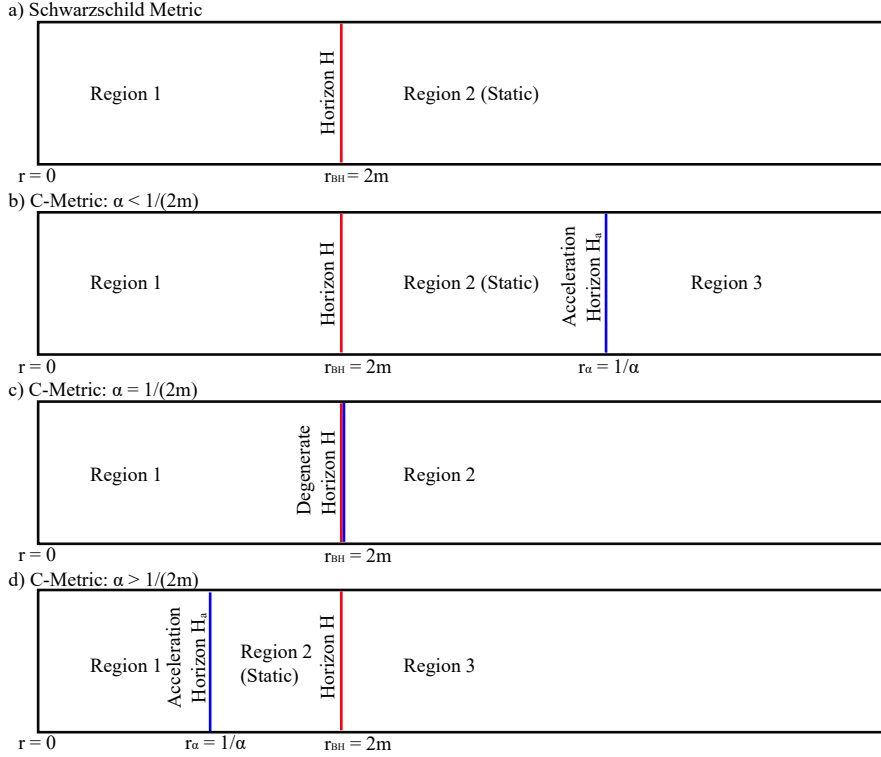


Figure 1. Position of the curvature singularity at $r = 0$ and the coordinate singularities in a) the Schwarzschild spacetime and the C-metric for b) $r_{BH} < r_\alpha$, c) $r_{BH} = r_\alpha$ and d) $r_\alpha < r_{BH}$. Note that the angular coordinates are suppressed and other singularities are not shown.

Then the only singularities we may encounter are the conical singularities on the axis. The string and the strut may be non-transparent or transparent. In the first case they will block lightlike geodesics and, thus, cast a shadow. In the second case lightlike geodesics will split into two when crossing the conic singularity: To see this, we consider a family of lightlike geodesics whose initial conditions depends continuously on a real parameter u . If the geodesics pass by the axis in positive φ direction for $u < 0$ and in negative φ direction for $u > 0$, the geodesic with $u = 0$ has two different continuations after crossing the axis. Note that this is different from the NUT metric which also features a conic singularity known as the Misner string: In the latter case geodesics are continuously differentiable when going through the string, without any splitting; therefore, it is quite natural in the NUT metric to assume that the string is transparent, as was also argued by Clément, Gal'tsov and Guenouche [29].

Since both the C-metric and the NUT metric belong to the family of Plebański-Demiański spacetimes [5], there is also a vacuum solution that combines both parameters. Griffiths and Podolský [30] have investigated this metric and shown that there is an ambiguity in the definition of the NUT parameter. Moreover, in 2006 Chng et al. [31] found another vacuum solution, not in the Plebański-Demiański class, that describes accelerating black holes with a NUT parameter and investigated its properties.

Podolský and Vrátný [32] extended this analysis and showed that for vanishing NUT charge the metric reduces to the classical C-metric.

Note that the domain of outer communication is time-symmetric. On the outer side it is bounded by a future acceleration horizon and by a past acceleration horizon, whereas on the inner side it is bounded by a future inner (black hole) horizon and by a past inner (white hole) horizon. We have already said that for our discussion of lensing features we have to consider only (sections of) lightlike geodesics that are confined to the domain of outer communication. However, if we extend such geodesics into the future they may cross one of the future horizons, and if we extend them into the past they may cross one of the past horizons. The *maximal* analytical extension of the C-metric actually describes two black holes that are accelerating in opposite directions, with their domains of outer communication being causally disconnected, see again Griffiths and Podolský [8]. However, this maximal extension is of no interest for the purpose of this paper.

3. Lightlike Geodesics

In this section we are going to solve the equations of motion for light rays in the C-metric. In general, the solutions are given in terms of elliptic integrals and elliptic functions which, for some special cases, simplify to elementary integrals and elementary functions. While in general there are different representations and different types of elliptic integrals and elliptic functions, in this paper we use the elliptic integrals of first and third kind in their canonical form as well as the Jacobian elliptic functions to solve the equations of motion. Since these may not be known to all readers we will define the elliptic integrals used in this paper and show how to use the Jacobian elliptic functions to solve differential equations in Appendices A and B.

We reduce the equations of motion for lightlike geodesics to first-order form with the help of constants of motion and we solve them with initial conditions $(x^\mu(\lambda = \lambda_i)) = (x_i^\mu) = (t_i, r_i, \vartheta_i, \varphi_i)$, where λ_i is the initial value of the Mino parameter. For the time being, we leave the initial values arbitrary. For explicit calculations we will later choose $\lambda_i = 0$, which is always possible, and also $t_i = 0$ and $\varphi_i = 0$, which is no restriction of generality because the metric is invariant under time translations and rotations about the axis of symmetry. We also have to bring to the reader's attention that although for $\alpha \rightarrow 0$ the geodesics of the C-metric reduce, of course, to the geodesics of the Schwarzschild metric, this is not always obvious from the expressions with $\alpha \neq 0$.

3.1. Equations of motion, photon sphere and photon cone

The equations of motion for lightlike geodesics are completely integrable. There are four constants of motion which allow us to rewrite the null geodesic equation in first order form: the Lagrangian $\mathcal{L} = 0$, the energy E , the z component of the angular momentum

L_z and the Carter constant K . The resulting first-order equations read

$$\frac{dt}{d\lambda} = \frac{r^2 E}{Q(r)}, \quad (7)$$

$$\frac{d\varphi}{d\lambda} = \frac{L_z}{P(\vartheta) \sin^2 \vartheta}, \quad (8)$$

$$\left(\frac{dr}{d\lambda}\right)^2 = r^4 E^2 - r^2 Q(r) K, \quad (9)$$

$$\left(\frac{d\vartheta}{d\lambda}\right)^2 = P(\vartheta) K - \frac{L_z^2}{\sin^2 \vartheta}. \quad (10)$$

Here λ is the Mino parameter [33]. It is related to an affine parameter s by

$$\frac{d\lambda}{ds} = \frac{\Omega(r, \vartheta)^2}{r^2}, \quad (11)$$

cf. e.g. eqs. (16) in Grenzebach et al. [18]. Note that $E \neq 0$ for all lightlike geodesics. Without loss of generality, we restrict to geodesics with $E > 0$ throughout this paper. According to (7) this is tantamount to requiring that the Mino parameter is future-directed with respect to the t coordinate.

From (10) we read that $K \geq 0$. Moreover, $K = 0$ implies $d\vartheta/d\lambda = 0$ and $L_z = 0$; by (8), the latter equation implies $d\varphi/d\lambda = 0$. This demonstrates that the null geodesics with $K = 0$ are ingoing or outgoing radial light rays. They are the principal null rays of the C-metric. (The dependence of their r and t coordinates on the Mino parameter will be given later). With the case $K = 0$ well understood, we may restrict in the following discussion to the case $K > 0$. We first discuss the ϑ motion. (10) may be rewritten as

$$\frac{\sin^2 \vartheta}{K} \left(\frac{d\vartheta}{d\lambda}\right)^2 + V_\vartheta(\vartheta) = -\frac{L_z^2}{K}, \quad (12)$$

where

$$V_\vartheta(\vartheta) = -P(\vartheta) \sin^2 \vartheta = -(1 - 2\alpha m \cos \vartheta) \sin^2 \vartheta. \quad (13)$$

(12) demonstrates that null geodesics with constants of motion L_z and K may exist only in the region where $V_\vartheta(\vartheta) < -L_z^2/K$, see figure 2. The potential $V_\vartheta(\vartheta)$ has a minimum at $\vartheta = \vartheta_{\text{ph}}$ given by

$$\cos \vartheta_{\text{ph}} = \frac{-2\alpha m}{1 + \sqrt{1 + 12\alpha^2 m^2}}. \quad (14)$$

The allowed values for L_z and K are

$$0 \geq -\frac{L_z^2}{K} \geq V_\vartheta(\vartheta_{\text{ph}}). \quad (15)$$

Null geodesics with $-L_z^2/K = V_\vartheta(\vartheta_{\text{ph}})$ are completely contained in the cone $\vartheta = \vartheta_{\text{ph}}$. Hereafter we will refer to it as the *photon cone*. Null geodesics with $L_z = 0$ meet the axis. All other null geodesics oscillate between a minimum value, $0 < \vartheta_{\text{min}} < \vartheta_{\text{ph}}$, and a maximum value, $\vartheta_{\text{ph}} < \vartheta_{\text{max}} < \pi$. Note that $\vartheta_{\text{ph}} \rightarrow \pi/2$ if $\alpha \rightarrow 0$ and $\vartheta_{\text{ph}} \rightarrow \arccos(-1/3) \approx 1.911$ if $\alpha \rightarrow 1/(2m)$.

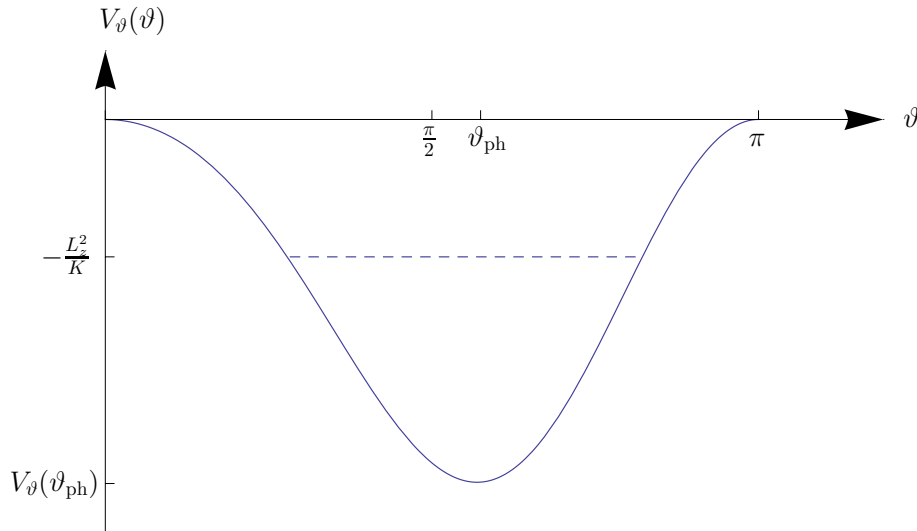


Figure 2. The potential $V_\vartheta(\vartheta)$ for latitudinal motion.

We now turn to the r motion. Eq. (9) may be rewritten as

$$\frac{1}{r^4 K} \left(\frac{dr}{d\lambda} \right)^2 + V_r(r) = \frac{E^2}{K}, \quad (16)$$

where

$$V_r(r) = \frac{Q(r)}{r^2} = \left(\frac{1}{r^2} - \alpha^2 \right) \left(1 - \frac{2m}{r} \right). \quad (17)$$

Null geodesics with constants of motion E and K exist in the domain where $V_r(r) \leq E^2/K$, see figure 3. The potential $V_r(r)$ has a maximum at $r = r_{\text{ph}}$ where

$$r_{\text{ph}} = \frac{6m}{1 + \sqrt{1 + 12\alpha^2 m^2}}. \quad (18)$$

Note that $r_{\text{ph}} \rightarrow 3m$ if $\alpha \rightarrow 0$ and $r_{\text{ph}} \rightarrow 2m$ if $\alpha \rightarrow 1/(2m)$. The sphere $r = r_{\text{ph}}$ is called the *photon sphere* or the *light sphere*. If a null geodesic is tangential to this sphere at one point, then it is completely contained in this sphere.

Null geodesics with $E^2/K < V_r(r_{\text{ph}})$ have exactly one extremum of the r motion which is either a maximum at a value $2m < r_{\text{max}} < r_{\text{ph}}$ or a minimum at a value $r_{\text{ph}} < r_{\text{min}} < 1/\alpha$. Null geodesics with $E^2/K > V_r(r_{\text{ph}})$ have no extremum of the r motion. Null geodesics with $E^2/K = V_r(r_{\text{ph}})$ are either completely contained in the photon sphere or they spiral asymptotically towards the photon sphere. Of all the null geodesics that fill the photon sphere, only the ones through the axis lie on halves of great circles. Whenever a null geodesic crosses the axis the φ coordinate of the half of the great circle changes and generally the halves before and after crossing the axis do not form a closed great circle (for more details see Section 3.4). At the intersection of $r = r_{\text{ph}}$ and $\vartheta = \vartheta_{\text{ph}}$ there is a circular null geodesic, but it is not a great circle. All the other null geodesics on the photon sphere are non-circular.

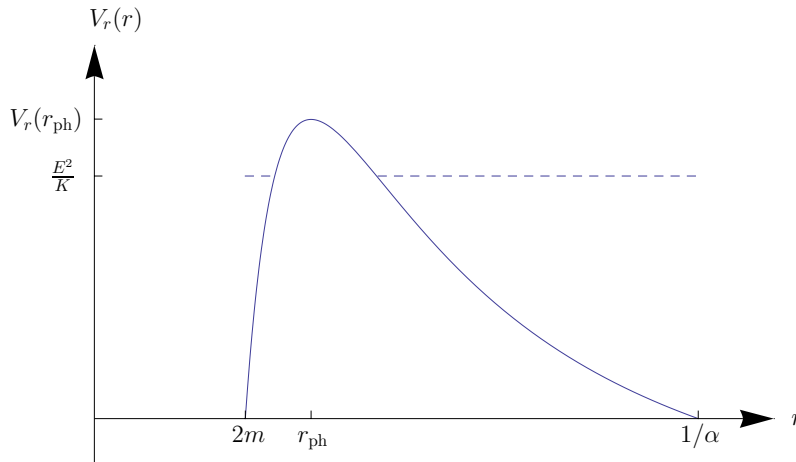


Figure 3. The potential $V_r(r)$ for radial motion.

The photon sphere is of crucial relevance for lensing, in particular for the formation of the shadow. This was discussed in detail, for a class of spacetimes that includes the C-metric, by Grenzebach et al. [18, 19]. It should be mentioned that the photon sphere is not a “round sphere”, i.e., its intrinsic geometry is not that of the standard sphere in Euclidean 3-space, see Gibbons and Warnick [21]. The photon cone appeared in the literature only recently: Alrais Alawadi et al. [22] found that there is a circular lightlike geodesic at the intersection of this cone with the photon sphere. (Note that their α is our $-\alpha$.) We believe that our characterisation of the photon cone in terms of the potential $V_\vartheta(\vartheta)$ is particularly transparent and gives additional useful information.

Having discussed some qualitative features of lightlike geodesics with the help of the potentials (13) and (17), we will now explicitly solve the equations of motion (7)-(10). Generically, this will be done in terms of elliptic integrals and elliptic functions. For some special geodesics the solutions reduce to elementary functions. For each of the four equations we will first characterise the special cases and then the generic ones.

3.2. The r motion

3.2.1. Types of motion The fourth-order polynomial on the right-hand side of (9) has always four roots r_1, r_2, r_3 and r_4 in the complex plane which can be determined, e.g., with Cardano’s method. Real roots in the interval between r_{BH} and r_α give turning points of the geodesic. Note that there is always a root at $r = 0$ and another one at some real value $r \leq 0$. The remaining two roots are either real and non-negative or non-real and complex conjugate to each other. We have to distinguish the special cases where two or more roots coincide from the generic cases where the four roots are distinct. This will give us four qualitatively different types of r motion. The roots depend, of course, on the constants of motion. Therefore, the four different types of r motion can be characterised in terms of the constants of motion. For this purpose it is convenient

to define a new constant of motion $K_E = \frac{K}{E^2}$ (recall that $E \neq 0$ for all lightlike geodesics and that we choose $E > 0$) and to introduce the abbreviation

$$K_{ph} = \frac{r_{ph}^2}{Q(r_{ph})}, \quad (19)$$

where r_{ph} is the radius of the photon sphere. We can then characterise the four types of r motion as follows:

- (i) $K_E = 0$: These are the principal null geodesics. The polynomial has four real roots all of which coincide, $r_1 = r_2 = r_3 = r_4 = 0$.
- (ii) $K_E = K_{ph}$: These are null geodesics on the photon sphere or asymptotically approaching the photon sphere in the future or in the past. The polynomial has four real roots two of which coincide; we label them such that $r_4 < r_3 = 0 < r_2 = r_1 = r_{ph}$.
- (iii) $K_{ph} < K_E$: In the domain $r_{BH} < r < r_{ph}$ these are geodesics with a maximum at $r_{max} = r_2$ and in the domain $r_{ph} < r < r_\alpha$ these are geodesics with a minimum at $r_{min} = r_1$. The polynomial has four distinct real roots which we label such that $r_4 < r_3 = 0 < r_2 < r_1$.
- (iv) $0 < K_E < K_{ph}$: These are null geodesics without turning points. The polynomial has four distinct roots two of which are real and two are complex conjugate; we label them such that $0 = r_1 > r_2$, $r_3 = R_3 + iR_4$ and $r_4 = R_3 - iR_4$ with R_3 real and R_4 positive.

We now discuss each of the four types of r motion separately.

3.2.2. Principal null geodesics: For principal null geodesics we have $K = 0$. In this case (9) reduces to

$$\left(\frac{dr}{d\lambda}\right)^2 = r^4 E^2. \quad (20)$$

With the initial condition $r(\lambda_i) = r_i$ and indicating the sign of $dr/d\lambda$ at λ_i by i_{r_i} we get as solution

$$r(\lambda) = \frac{r_i}{1 - i_{r_i} r_i E(\lambda - \lambda_i)}. \quad (21)$$

3.2.3. Geodesics with $K_E = K_{ph}$: When we have $K_E = K_{ph}$ (9) has a double zero at $r = r_{ph}$. Therefore we have either null geodesics that are trapped on the photon sphere or null geodesics that asymptotically come from or go to the photon sphere. In the former case the solution is trivial, $r(\lambda) = r_i = r_{ph}$. In the latter case we substitute

$$r = \frac{6mK}{12y + K} \quad (22)$$

in (9) and obtain

$$\left(\frac{dy}{d\lambda}\right)^2 = 4y^3 - g_{2,r}y - g_{3,r}. \quad (23)$$

Here, $g_{2,r}$ and $g_{3,r}$ are constants of motion that can be expressed in terms of m , α , E and K . The explicit form of these expressions need not be given here. Expressing the polynomial in terms of its roots we obtain:

$$\left(\frac{dy}{d\lambda}\right)^2 = 4(y - y_{ph})^2(y - y_1). \quad (24)$$

y_{ph} and y_1 are related to r_{ph} and r_4 via (22). Using this transformation it is easy to show that we have $y_{ph} < y$ for $r_{BH} < r < r_{ph}$, and $y < y_{ph}$ for $r_{ph} < r < r_\alpha$. Similarly one can easily show that $y_1 < y_{ph}$ and $y_1 < y$.

Now separation of variables and integrating from $y(\lambda_i) = y_i$ to $y(\lambda)$ leads to

$$\lambda - \lambda_i = -\frac{i_{r_i}}{2} \int_{y_i}^y \frac{dy'}{\sqrt{(y' - y_{ph})^2(y' - y_1)}}. \quad (25)$$

Here we have to distinguish null geodesics between the black hole horizon and the photon sphere from null geodesics between the photon sphere and the acceleration horizon. In the former case we have $y_{ph} < y$ ($r_{BH} < r < r_{ph}$) and rewrite the right-hand side using I_1 in (A.1). In the latter case we have $y < y_{ph}$ ($r_{ph} < r < r_\alpha$) and rewrite the right-hand side using I_2 in (A.1).

For $r_{BH} < r < r_{ph}$ we now integrate following the steps in Appendix A.1 and obtain (A.2). After inserting in (25) and solving for r we obtain

$$r(\lambda) = \frac{r_{ph}r_4}{r_{ph} - (r_{ph} - r_4) \coth^2 \left(\operatorname{arcoth} \left(\sqrt{\frac{r_{ph}(r_i - r_4)}{r_i(r_{ph} - r_4)}} \right) + i_{r_i} \sqrt{\frac{mK(r_4 - r_{ph})}{2r_{ph}r_4}} (\lambda - \lambda_i) \right)}. \quad (26)$$

Following the analogous steps for $r_{ph} < r < r_\alpha$ we get (A.3). This time solving for r leads to

$$r(\lambda) = \frac{r_{ph}r_4}{r_{ph} - (r_{ph} - r_4) \tanh^2 \left(\operatorname{artanh} \left(\sqrt{\frac{r_{ph}(r_i - r_4)}{r_i(r_{ph} - r_4)}} \right) - i_{r_i} \sqrt{\frac{mK(r_4 - r_{ph})}{2r_{ph}r_4}} (\lambda - \lambda_i) \right)}. \quad (27)$$

3.2.4. Geodesics with $K_{ph} < K_E$: Again we have to distinguish null geodesics between the black hole horizon r_{BH} and the photon sphere r_{ph} from null geodesics between the photon sphere r_{ph} and the acceleration horizon r_α . In the former case the geodesic has a turning point at $r_{max} = r_2$. In this case we use the transformation [34, 27]

$$r = r_1 - \frac{r_1(r_1 - r_2)}{r_1 - r_2 \sin^2 \chi_r} \quad (28)$$

to put (9) into the Legendre form (B.1). Now we follow the steps described in Appendix B to obtain the solution for $r(\lambda)$ in terms of Jacobi's sn function:

$$r(\lambda) = r_1 - \frac{r_1(r_1 - r_2)}{r_1 - r_2 \operatorname{sn}^2 \left(i_{r_i} \frac{\sqrt{(E^2 + \alpha^2 K)r_1(r_2 - r_4)}}{2} (\lambda_i - \lambda) + \lambda_{r_i, k_1}, k_1 \right)}. \quad (29)$$

Here, k_1 and λ_{r_i, k_1} are given by the following two relations:

$$k_1 = \frac{r_2(r_1 - r_4)}{r_1(r_2 - r_4)}, \quad (30)$$

$$\lambda_{r_i, k_1} = F_L(\chi_{r,i}, k_1), \chi_{r,i} = \arcsin \left(\sqrt{\frac{(r_2 - r_i)r_1}{(r_1 - r_i)r_2}} \right). \quad (31)$$

Analogously for null geodesics between the photon sphere r_{ph} and the acceleration horizon r_α we use the transformation [34, 27]

$$r = r_2 + \frac{(r_1 - r_2)(r_2 - r_4)}{r_2 - r_4 - (r_1 - r_4) \sin^2 \chi_r} \quad (32)$$

to put (9) into the Legendre form (B.1). Again we follow the procedure described in Appendix B and obtain the solution for $r(\lambda)$, which again involves Jacobi's sn function and this time reads

$$r(\lambda) = r_2 + \frac{(r_1 - r_2)(r_2 - r_4)}{r_2 - r_4 - (r_1 - r_4) \operatorname{sn}^2 \left(i_{r_i} \frac{\sqrt{(E^2 + \alpha^2 K)r_1(r_2 - r_4)}}{2} (\lambda - \lambda_i) + \lambda_{r_i, k_1}, k_1 \right)}, \quad (33)$$

where

$$\lambda_{r_i, k_1} = F_L(\chi_{r,i}, k_1), \chi_{r,i} = \arcsin \left(\sqrt{\frac{(r_i - r_1)(r_2 - r_4)}{(r_i - r_2)(r_1 - r_4)}} \right). \quad (34)$$

3.2.5. Geodesics with $0 < K_E < K_{ph}$: Null geodesics with $0 < K_E < K_{ph}$ do not possess turning points. Therefore in this case we only need one transformation to put (9) into the Legendre form. Using the real root r_2 and the real and imaginary parts R_3 and R_4 of the complex conjugate roots r_3 and r_4 we first define two new constants of motion R and \bar{R} given by

$$R = \sqrt{R_3^2 + R_4^2}, \text{ and } \bar{R} = \sqrt{(R_3 - r_2)^2 + R_4^2}. \quad (35)$$

Now we use the transformation [34, 27]

$$r = \frac{r_2 R (\cos \chi_r - 1)}{\bar{R} - R + (\bar{R} + R) \cos \chi_r}, \quad (36)$$

to put (9) in the Legendre form (B.1). Again we follow the steps described in Appendix B. This time the solution for $r(\lambda)$ is given in terms of Jacobi's cn function. It reads

$$r(\lambda) = \frac{r_2 R \left(\operatorname{cn} \left(i_{r_i} \sqrt{(E^2 + \alpha^2 K) R \bar{R}} (\lambda - \lambda_i) + \lambda_{r_i, k_2}, k_2 \right) - 1 \right)}{\bar{R} - R + (\bar{R} + R) \operatorname{cn} \left(i_{r_i} \sqrt{(E^2 + \alpha^2 K) R \bar{R}} (\lambda - \lambda_i) + \lambda_{r_i, k_2}, k_2 \right)}, \quad (37)$$

where k_2 and λ_{r_i, k_2} are given by

$$k_2 = \frac{(R + \bar{R})^2 - r_2^2}{4R\bar{R}}, \quad (38)$$

$$\lambda_{r_i, k_2} = F_L(\chi_{r,i}, k_2) \text{ and } \chi_{r,i} = \arccos \left(\frac{(r_i - r_2)R - r_i \bar{R}}{(r_i - r_2)R + r_i \bar{R}} \right). \quad (39)$$

3.3. The ϑ Motion

For discussing the ϑ motion it is convenient to rewrite (10) as a differential equation for $x = \cos \vartheta$,

$$\left(\frac{dx}{d\lambda}\right)^2 = (1-x^2)(1-2\alpha mx)K - L_z^2. \quad (40)$$

We immediately see that when we have $K = L_z^2 = 0$ the right-hand side vanishes identically. In all other cases the third-order polynomial on the right-hand side must have three real roots because, as discussed in Section 3.1, we always have two turning points. Using this information we can now distinguish the following three types of ϑ motion:

- (i) $K = L_z^2 = 0$: These are again the principal null geodesics. The right-hand side of (40) vanishes identically.
- (ii) $K = \frac{L_z^2}{\sin^2 \vartheta_{ph} P(\vartheta_{ph})} \neq 0$: These are null geodesics on the photon cone. Two of the three real roots coincide; we label them such that $x_1 > x_2 = x_3 = \cos \vartheta_{ph}$.
- (iii) $K \neq \frac{L_z^2}{\sin^2 \vartheta_{ph} P(\vartheta_{ph})}$: These are null geodesics where the ϑ coordinate oscillates between a minimum and a maximum. The three real roots are distinct; we label them such that $x_3 < x_2 < x_1$ where $x_2 = \cos \vartheta_{\min}$ and $x_3 = \cos \vartheta_{\max}$.

For (i) and (ii) (40) is easy to solve. In both cases we have $\frac{dx}{d\lambda} = \frac{d^2x}{d\lambda^2} = 0$ and thus $x = \cos \vartheta = \text{const}$. Thus in both cases the solution is $\vartheta(\lambda) = \vartheta_i$.

Now we turn to case (iii). Here we first transform (40) to the Legendre form (B.1) using the following coordinate transformation [34]:

$$x = \cos \vartheta = (x_2 - x_3) \sin^2 \chi_\vartheta + x_3. \quad (41)$$

As for the r motion we follow the steps in Appendix B to solve the differential equation and obtain the solution for $\vartheta(\lambda)$ in terms of Jacobi's sn function:

$$\vartheta(\lambda) = \arccos \left((x_2 - x_3) \text{sn}^2 \left(i_{\vartheta_i} \sqrt{\frac{\alpha m K (x_1 - x_3)}{2}} (\lambda_i - \lambda) + \lambda_{\vartheta_i, k_3}, k_3 \right) + x_3 \right). \quad (42)$$

Here, i_{ϑ_i} denotes the sign of $d\vartheta/d\lambda$ at λ_i . The square of the elliptic modulus k_3 and $\lambda_{\vartheta_i, k_3}$ are given by

$$k_3 = \frac{x_2 - x_3}{x_1 - x_3}, \text{ and } \lambda_{\vartheta_i, k_3} = F_L(\chi_{\vartheta, i}, k_3), \chi_{\vartheta, i} = \arcsin \left(\sqrt{\frac{\cos \vartheta_i - x_3}{x_2 - x_3}} \right). \quad (43)$$

3.4. The φ motion

As the right-hand side of (8) is known once we have calculated $\vartheta(\lambda)$, the φ motion is determined by the ϑ motion. Therefore the different types of φ motion correspond to the different types of the ϑ motion:

- (i) $K = L_z^2 = 0$: These are the principal null geodesics for which the right-hand side of (8) vanishes. So for these geodesics we have $\varphi(\lambda) = \varphi_i$.

- (ii) $K = \frac{L_z^2}{\sin^2 \vartheta_{ph} P(\vartheta_{ph})} \neq 0$: These are null geodesics on the photon cone. For them the right-hand side of (8) is constant, so the solution is

$$\varphi(\lambda) = \varphi_i + \frac{L_z(\lambda - \lambda_i)}{P(\vartheta_{ph}) \sin^2 \vartheta_{ph}}. \quad (44)$$

- (iii) $K \neq \frac{L_z^2}{\sin^2 \vartheta_{ph} P(\vartheta_{ph})}$: Here the geodesics with $L_z = 0$ have to be considered separately. These are geodesics which meet the axis $\sin \vartheta = 0$. If the string and the strut are non-transparent, then these geodesics are blocked at the axis. Otherwise they split into two geodesics which can be calculated by continuously extending sequences of geodesics with positive and negative L_z , respectively. For the null geodesics with $L_z \neq 0$ we proceed similarly to the ϑ motion. We first rewrite the right-hand side of (8) in terms of the variable $x = \cos \vartheta$:

$$\frac{d\varphi}{d\lambda} = \frac{L_z}{(1-x^2)(1-2\alpha mx)}. \quad (45)$$

After dividing (45) by $\pm dx/d\lambda$ and substituting for the latter from (40) the resulting equation can be integrated:

$$\varphi(\lambda) = \varphi_i + \int_{\cos \vartheta_i \dots}^{\dots \cos \vartheta(\lambda)} \frac{L_z dx}{(1-x^2)(1-2\alpha mx) \sqrt{(1-x^2)(1-2\alpha mx)K - L_z^2}}. \quad (46)$$

Here the dots indicate that we have to split the integral at each turning point, choosing the sign of $\pm dx/d\lambda$ such that $L_z^{-1} d\varphi/d\lambda$ is always positive. Next we perform a partial fraction decomposition of $(1-x^2)^{-1}(1-2\alpha mx)^{-1}$. Then we use (41) and express (46) by elliptic integrals of the third kind (A.4).

3.5. The time coordinate t

For calculating the time coordinate t as a function of λ we have to distinguish the same four types of motion as for the radius coordinate r . In all cases but one we start with (7) and divide by $\pm dr/d\lambda$ as given by (9). Next we integrate and obtain

$$t(\lambda) = t_i + \int_{r_i \dots}^{\dots r(\lambda)} \frac{Er'^2 dr'}{Q(r') \sqrt{r'^4 E^2 - r'^2 Q(r') K}}. \quad (47)$$

Here the dots indicate that we have to split the integral at a turning point and to choose the sign of $\pm dr/d\lambda$ such that $dt/d\lambda$ is always positive.

3.5.1. Principal null geodesics We first set $K = 0$ in (47). Then we re-arrange the term $Q(r)^{-1}$ such that only terms with r in the denominator remain and perform a partial fraction decomposition. This leaves us with three elementary integrals that can be easily evaluated,

$$t(\lambda) = t_i + i_{r_i} \left(\frac{2m}{1-4\alpha^2 m^2} \ln \left(\frac{r(\lambda) - 2m}{r_i - 2m} \right) + \frac{1}{2\alpha(1-2\alpha m)} \ln \left(\frac{1 - \alpha r_i}{1 - \alpha r(\lambda)} \right) + \frac{1}{2\alpha(1+2\alpha m)} \ln \left(\frac{1 + \alpha r(\lambda)}{1 + \alpha r_i} \right) \right). \quad (48)$$

Note that this is the same expression as derived by Lim [17]. The only difference is that we expressed the integration constant in terms of the initial conditions.

3.5.2. Geodesics with $K_E = K_{ph}$ The first case we have to consider are null geodesics on the photon sphere. For these geodesics we have $r = r_{ph} = \text{const.}$ In this case inserting r_{ph} into (7) and integrating over λ yields:

$$t(\lambda) = t_i + \frac{r_{ph}^2 E(\lambda - \lambda_i)}{Q(r_{ph})}. \quad (49)$$

In the second case we have null geodesics asymptotically coming from or going to the photon sphere. Here, we first substitute (22) into (47) and perform a partial fraction decomposition. Now we split the integral into four different terms. After expressing (47) using the integrals from Appendix A.1 we find:

$$t(\lambda) = t_i \pm i_{r_i} \left(\frac{2r_{ph}m^2 EI_{ph,1}}{(1 - 4\alpha^2 m^2)(r_{ph} - 2m)} - \frac{r_{ph} EI_{ph,2}}{4\alpha(1 - 2\alpha m)(1 - \alpha r_{ph})} \right. \\ \left. + \frac{r_{ph} EI_{ph,3}}{4\alpha(1 + 2\alpha m)(1 + \alpha r_{ph})} \mp \frac{r_{ph}^3 EI_{ph,4\pm}}{2(r_{ph} - 2m)(1 - \alpha^2 r_{ph}^2)} \right). \quad (50)$$

Here, the upper sign is valid for null geodesics between the photon sphere and the acceleration horizon, while the lower sign is valid for null geodesics between the black hole horizon and the photon sphere. The integrals $I_{ph,1}$ - $I_{ph,4\pm}$ in (50) are given by (A.2) and (A.3) in Appendix A.1.

3.5.3. Geodesics with $K_{ph} < K_E$ Here we proceed as for principal null geodesics. We first rewrite (47) such that it only contains r in the denominator. Then we perform a partial fraction decomposition. For null geodesics between the photon sphere and the acceleration horizon we now use (32) to rewrite (47) using elliptic integrals of first and third kind. Analogously for null geodesics between the black hole horizon and the photon sphere we use (28) to rewrite (47) using elliptic integrals of first and third kind. In the former case the parameter of the elliptic integral of third kind is > 1 for the term diverging at the acceleration horizon while in the latter case it is > 1 for the term diverging at the black hole horizon. However, in both cases we chose the coordinate transformations such that we never integrate over these divergences.

3.5.4. Geodesics with $0 < K_E < K_{ph}$ The first steps are the same as for null geodesics with $K_{ph} < K_E$. After the partial fraction decomposition we use (36) and rewrite (47) using elliptic integrals of first kind and the non-standard elliptic integral $J(\chi_i, \chi, k, n)$. The latter we now rewrite as (A.6) using elliptic integrals of third kind and elementary functions as demonstrated in Appendix A.2. Note that for the term diverging at the black hole horizon we always integrate over the divergence and thus for this term we have to rewrite the elliptic integrals of third kind using (A.8).

3.6. Calculation and visualisation of the analytically determined null geodesics

For the visualisation of the null geodesics we implemented all solutions in the programming language Julia [35]. Because it is a common convention that general null geodesics are future-directed we will limit our description of the calculation procedure to future-directed null geodesics. Whenever differences to past-directed null geodesics occur – which we have to use when we turn to gravitational lensing in Section 4 – we write them in brackets directly behind the expression for future-directed null geodesics. For most of the calculations the procedure is straight forward and can be applied to future-directed and past-directed null geodesics alike. We set $\lambda_i = 0$, $t_i = 0$ and $\varphi_i = 0$. For any choice of r_i , ϑ_i , E , L_z and K we integrate the equations of motion from $\lambda_i = 0$ up to some value $\lambda_f > 0$ for future-directed null geodesics and $\lambda_f < 0$ for past-directed null geodesics. The formulas derived in the preceding sections give us directly $r(\lambda_f)$ and $\vartheta(\lambda_f)$. For calculating $t(\lambda_f)$ with the help of (47) we need to know the turning points of the r motion between $\lambda_i = 0$ and λ_f , and for calculating $\varphi(\lambda_f)$ with the help of (46) we need to know the turning points of the ϑ motion between $\lambda_i = 0$ and λ_f . We know that the r motion can have only one turning point; between $\lambda_i = 0$ and $\lambda_f > 0$ (for past-directed null geodesics: $\lambda_f < 0$) such a turning point is necessarily a maximum for initially outgoing geodesics, given by (29), while it is necessarily a minimum for initially ingoing geodesics, given by (33). By contrast, the ϑ motion can potentially have arbitrarily many turning points.

For determining $t(\lambda_f)$ we proceed in the following way. For an initially outgoing geodesic with a maximum of the r motion we have to check whether this maximum r_{\max} comes before λ_f . To that end we solve (9) for $d\lambda/dr$ and integrate from r_i to r_{\max} . This gives us the Mino parameter λ_{\max} at the maximum as an elliptic integral of the first kind. If $\lambda_{\max} < \lambda_f$ (for past-directed null geodesics: $\lambda_{\max} > \lambda_f$), we have to split the integral (47) into two sections, from λ_i to λ_{\max} and from λ_{\max} to λ_f ; otherwise, we just have to integrate from λ_i to λ_f . For an initially ingoing geodesic with a minimum of the r motion the procedure is analogous.

Determining $\varphi(\lambda_f)$ is more awkward because the ϑ motion may have arbitrarily many turning points. For determining the values of the Mino parameters $\lambda_{\text{turn},1}$, $\lambda_{\text{turn},2}$ etc. that lie in the interval between $\lambda_i = 0$ and λ_f we solve (40) for $d\lambda/dx$ and integrate from $x_i = \cos\vartheta_i$ up to the first turning point $x_{\text{turn},1}$. This is an elliptic integral of the first kind that gives us $\lambda_{\text{turn},1}$. Integrating the same expression from one turning point $x_{\text{turn},k}$ up to the next $x_{\text{turn},(k+1)}$ gives us the difference $\Delta\lambda = \lambda_{\text{turn},(k+1)} - \lambda_{\text{turn},k}$. Note that this difference is independent of k . Then we get $\varphi(\lambda_f)$ from (46) where we have to break the integral at each value $\lambda_{\text{turn},1}$, $\lambda_{\text{turn},2} = \lambda_{\text{turn},1} + \Delta\lambda$, $\lambda_{\text{turn},3} = \lambda_{\text{turn},1} + 2\Delta\lambda$ etc. that is smaller than λ_f (for past-directed null geodesics: bigger than λ_f).

In figure 4 we visualise two null geodesics. The blue geodesic is a null geodesic on the photon sphere. We can see that it propagates back and forth between the turning points of the ϑ motion while it precesses around the photon sphere without crossing the axis. For special initial conditions the φ motion and the ϑ motion have commensurable

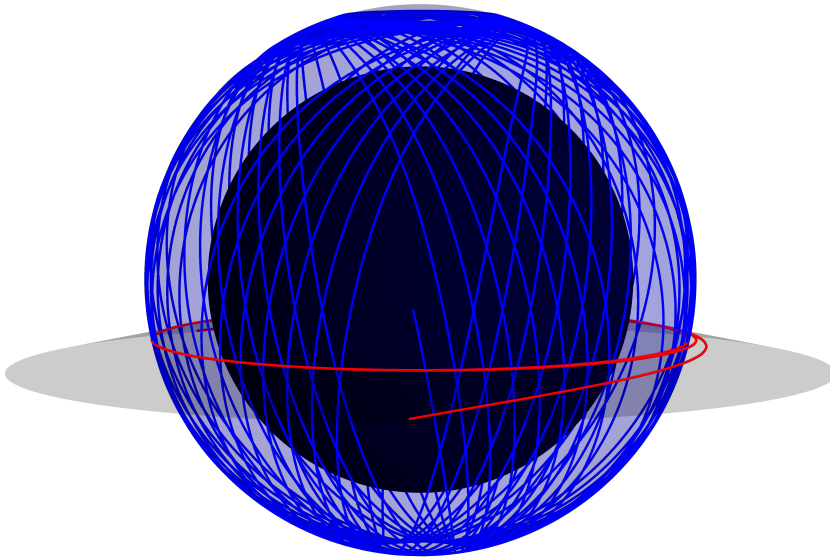


Figure 4. Examples for two geodesics in the C-metric with acceleration parameter $\alpha = 1/(4m)$. In the plot we use standard spherical coordinates. The blue geodesic is a null geodesic on the photon sphere with $r_i = r_{ph}$, $\vartheta_i = \pi/2$ and $\varphi_i = 0$. The red geodesic is a geodesic on the photon cone with $r_i = 3.9m$, $\vartheta_i = \vartheta_{ph}$ and $\varphi_i = 0$.

periods; then the geodesic is closed. For generic initial conditions, the geodesic fills part of the photon sphere densely. Note that the asymmetry with respect to the equatorial plane is clearly visible. – The red geodesic is a null geodesic on the photon cone for which the r coordinate has a minimum r_{\min} in close proximity to the photon sphere. If maximally extended, this geodesic enters into the domain of outer communication over the past acceleration horizon and leaves it over the future acceleration horizon.

4. Gravitational lensing in the C-metric

4.1. Celestial coordinates

Following the usual astronomical convention, we use latitude-longitude coordinates on the celestial sphere of an observer. For this purpose we first fix a static observer at the coordinates $(x_O^\mu) = (t_O, r_O, \vartheta_O, \varphi_O)$ between the black hole horizon r_{BH} and the acceleration horizon r_α . Because of the symmetry of the spacetime, it is irrelevant which values we choose for t_O and φ_O . At the position of the observer we now introduce an orthonormal tetrad following Grenzebach et al. [18, 19]:

$$e_0 = \frac{\Omega(r, \vartheta)}{\sqrt{Q(r)}} \partial_t \Big|_{(x_O^\mu)}, \quad (51)$$

$$e_1 = \frac{\Omega(r, \vartheta) \sqrt{P(\vartheta)}}{r} \partial_\vartheta \Big|_{(x_O^\mu)}, \quad (52)$$

$$e_2 = - \frac{\Omega(r, \vartheta)}{r \sin \vartheta \sqrt{P(\vartheta)}} \partial_\varphi \Big|_{(x_O^\mu)}, \quad (53)$$

$$e_3 = - \Omega(r, \vartheta) \sqrt{Q(r)} \partial_r \Big|_{(x_O^\mu)}. \quad (54)$$

In general the tangent vector of a null geodesic in Mino parameterisation, $\eta(\lambda)$, is given by:

$$\frac{d\eta}{d\lambda} = \frac{dt}{d\lambda} \partial_t + \frac{dr}{d\lambda} \partial_r + \frac{d\vartheta}{d\lambda} \partial_\vartheta + \frac{d\varphi}{d\lambda} \partial_\varphi. \quad (55)$$

Introducing celestial coordinates Σ (latitude) and Ψ (longitude) at the position of the observer the tangent vector can also be written as:

$$\frac{d\eta}{d\lambda} = \sigma (-e_0 + \sin \Sigma \cos \Psi e_1 + \sin \Sigma \sin \Psi e_2 + \cos \Sigma e_3). \quad (56)$$

The factor σ is a normalisation constant given by:

$$\sigma = g \left(\frac{d\eta}{d\lambda}, e_0 \right). \quad (57)$$

According to our convention of considering only lightlike geodesics with $E > 0$, the factor σ has to be negative. Note that the Mino parameter is defined only up to an affine transformation. Therefore, we can assume without loss of generality that $\sigma = -r_O^2 / \Omega(r_O, \vartheta_O)^2$. Then comparing the coefficients yields the constants of motion:

$$E = \frac{\sqrt{Q(r_O)}}{\Omega(r_O, \vartheta_O)}, \quad L_z = \frac{r_O \sqrt{P(\vartheta_O)} \sin \vartheta_O \sin \Sigma \sin \Psi}{\Omega(r_O, \vartheta_O)}, \quad K = \frac{r_O^2 \sin^2 \Sigma}{\Omega(r_O, \vartheta_O)^2}. \quad (58)$$

4.2. Angular radius of the shadow

For the (idealised) definition of the shadow of a black hole we assume that there are light sources everywhere in the universe but not between the observer and the black hole. From the position of the observer, who is assumed to be in the domain of outer communication, we follow all lightlike geodesics backwards in time. Note that according to our conventions the Mino parameter *decreases* along such geodesics. There are two types of such geodesics: Those which go towards the inner horizon and those which go to the outer horizon. As the former will not meet a light source, according to our assumption, we associate darkness with their initial directions. By contrast, the latter will meet a light source, so we associate brightness with their initial directions. Therefore, the boundary of the dark region, which is called the shadow, is determined by light rays that go to neither of the horizons. Each of these light rays is asymptotically spiralling towards a lightlike geodesic that is contained in the photon sphere, so it must have the same constants of motion as the limiting lightlike geodesic. For the limiting geodesic (9) has to hold with the left-hand side equal to zero and with $r = r_{ph}$ inserted

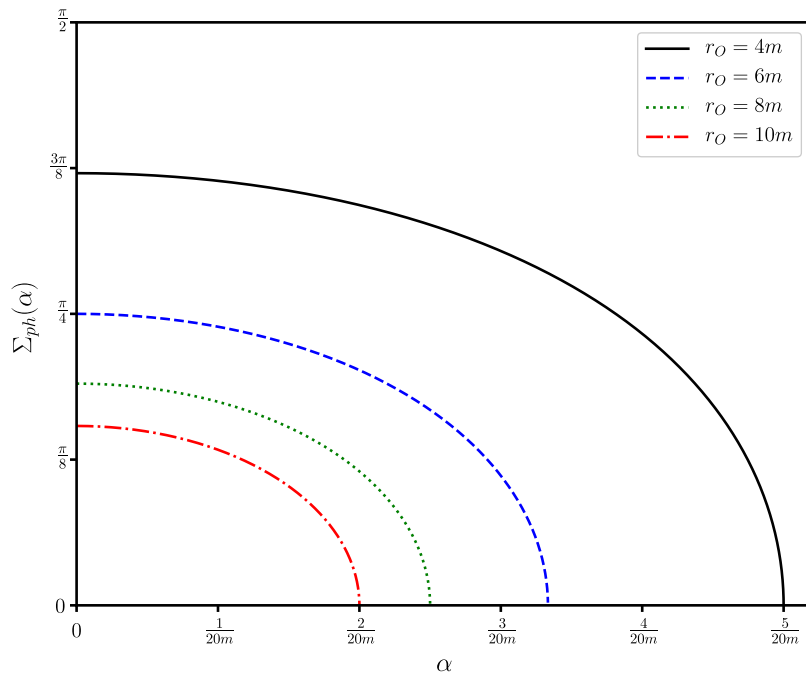


Figure 5. Angular radius of the shadow for varying α for observers located at $r_O = 4m$ (solid black line), $r_O = 6m$ (dashed blue line), $r_O = 8m$ (dotted green line), and $r_O = 10m$ (dash-dotted red line). Note that Σ_{ph} does not depend on ϑ_O .

on the right-hand side. On the other hand, the constants of motion of the spiralling geodesic must satisfy (58). Combining these two observations and solving for $\Sigma = \Sigma_{ph}$ gives the angular radius of the shadow:

$$\Sigma_{ph} = \arcsin \left(\frac{r_{ph}}{r_O} \sqrt{\frac{Q(r_O)}{Q(r_{ph})}} \right). \quad (59)$$

This agrees with the result of Grenzebach et al. [18] if the latter is specified to the case of vanishing spin and vanishing NUT parameter. Note that (59) reduces to Synge's formula [36] in the Schwarzschild limit ($\alpha \rightarrow 0$).

Here it is remarkable that we get an expression for $\Sigma = \Sigma_{ph}$ that does not involve Ψ . Therefore, the shadow is circular. This could not have been anticipated before the calculation was done because the C-metric is not spherically symmetric. Similarly Grenzebach et al. [37, 18] discovered that the shadow of a rotating black hole with NUT charge or acceleration is always symmetric to the equator on the observer's celestial sphere independent of the latitude ϑ_O of the observer. This is also not intrinsically obvious. While we do not have an explicit physical explanation for this fact, it is very likely that in both cases it can be attributed to the existence of the Carter constant K for lightlike geodesics and thus to the associated hidden symmetry.

In figure 5 we show Σ_{ph} for different radius coordinates r_O of the observer. As one would expect, the angular radius of the shadow decreases with increasing r_O and with

increasing acceleration parameter. The latter observation reflects the fact that, if r_O is kept fixed, with increasing α the acceleration horizon moves closer to the observer.

We have calculated the shadow for a static observer, i.e., we have assumed that the 4-velocity of the observer is parallel to ∂_t . From this result the shadow for a moving observer follows immediately by applying, on the tangent space at each point, the special-relativistic aberration formula, cf. Grenzebach [38]. As the aberration formula maps circles onto circles, the shadow is circular for *every* observer.

In view of observations, it is unfortunate that in the C-metric the shadow is circular. Therefore, we cannot distinguish the C-metric from the Schwarzschild spacetime, or from any other spherically symmetric black-hole spacetime, by the *shape* of the shadow. It is true that the acceleration parameter has an effect on the *size* of the shadow. This, however, cannot be utilised as long as one does not know the value of r_O with high accuracy. Other lensing features by which the C-metric could be distinguished from the Schwarzschild metric will be discussed in the following subsections.

4.3. The lens equation

A lens equation, or lens map, for an arbitrary general-relativistic spacetime was brought forward by Frittelli and Newman [39]. For spherically symmetric and static spacetimes, this lens equation was specified by Perlick [40]. In the following we apply the methodology of the latter paper to the C-metric. As the C-metric is not spherically symmetric, this requires some modifications.

We first distribute static light sources on the two sphere S_L^2 with radius coordinate $r_L > r_O$. Then we construct the past light cone for the static observer at the coordinates (x_O^μ) . We follow all null geodesics from the observer backwards in time until they intersect the two sphere S_L^2 . Again, we emphasise that according to our conventions the Mino parameter *decreases* along such geodesics. In general not all such geodesics intersect S_L^2 but for those which do we can construct the lens equation as defining a map from the angular coordinates Σ and Ψ on the observer's celestial sphere to the angular coordinates $\vartheta_L(\Sigma, \Psi)$ and $\varphi_L(\Sigma, \Psi)$ on the sphere of the light sources:

$$(\Sigma, \Psi) \rightarrow (\vartheta_L(\Sigma, \Psi), \varphi_L(\Sigma, \Psi)). \quad (60)$$

So the lens map is a map from part of a 2-sphere to a 2-sphere. In contrast to the spherically symmetric case which was treated by Perlick [40], this map is not rotationally symmetric, i.e., it does not reduce to a map from one angle to another angle.

We calculate $\vartheta_L(\Sigma, \Psi)$ and $\varphi_L(\Sigma, \Psi)$ from the analytic solutions of the equations of motion presented in the last section by setting $(x_i^\mu) = (x_O^\mu)$. Note that in this way we get a fully analytic lens map. The only unknown we have to eliminate is the Mino parameter λ_L of the geodesic when it meets the sphere at r_L . (Without loss of generality, we assume that all geodesics start at $\lambda_O = 0$ from the observer's position and end at $\lambda_L < \lambda_O$ at the position of the light source.) Since we fixed the radius coordinates r_O and r_L of the observer and of the light sources, respectively, we can use them to calculate λ_L . For this purpose we first express E and K in (9) by (58). Then we integrate and

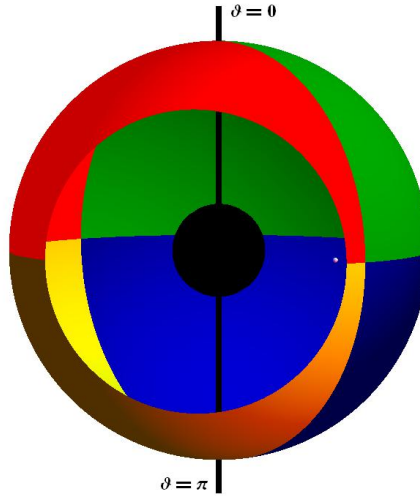


Figure 6. Sphere with radius r_L on which the light sources are distributed. The black ball is the horizon, the vertical black lines are the string and the strut, and the white dot marks the position of the observer (here at $r_O = 8m$, $\vartheta_O = \pi/2$ and $\varphi_O = 0$). What the observer sees is the inner side of the sphere with radius r_L . The colours represent the following coordinate ranges. $0 \leq \varphi_L < \pi$ and $0 \leq \vartheta_L \leq \pi/2$: green; $0 \leq \varphi_L < \pi$ and $\pi/2 < \vartheta_L \leq \pi$: blue; $\pi \leq \varphi_L < 2\pi$ and $0 \leq \vartheta_L \leq \pi/2$: red; $\pi \leq \varphi_L < 2\pi$ and $\pi/2 < \vartheta_L \leq \pi$: yellow. The outer side of the sphere is shown darkened in the picture because of lighting.

obtain λ_L . Here we have to distinguish the case with a turning point from the case without turning point. We will assume that r_O and r_L are both bigger than r_{ph} . Then a turning point cannot be a maximum. For null geodesics with a minimum as a turning point λ_L reads

$$\lambda_L = \left(\int_{r_O}^{r_{min}} - \int_{r_{min}}^{r_L} \right) \frac{\Omega(r_O, \vartheta_O) dr'}{\sqrt{Q(r_O)r'^4 - r_O^2 \sin^2 \Sigma r'^2 Q(r')}}}, \quad (61)$$

while for null geodesics without turning points it reads:

$$\lambda_L = - \int_{r_O}^{r_L} \frac{\Omega(r_O, \vartheta_O) dr'}{\sqrt{Q(r_O)r'^4 - r_O^2 \sin^2 \Sigma r'^2 Q(r')}}}. \quad (62)$$

As before we can rewrite the integral on the right-hand side (which, for some special cases, reduces to an elementary integral) as an elliptic integral of the first kind. After having calculated the Mino parameter we then proceed as described in section 3.6 to calculate $\vartheta_L(\Sigma, \Psi)$ and $\varphi_L(\Sigma, \Psi)$.

Figures 7-9 show the lens map for different observer positions in the C-metric with $\alpha = 1/(10m)$. The celestial sphere of the observer is represented in stereographic projection, with the direction towards the black hole at the centre. We have chosen the values $r_O = 8m$, $r_L = 9m$, $\vartheta_O = \pi/4$ (figure 7), $\vartheta_O = \pi/2$ (figure 8) and $\vartheta_O = 3\pi/4$ (figure 9). The sphere at r_L is divided into four quarter-spheres which are painted red, green, blue and yellow, respectively, see figure 6. This colouring follows the convention in

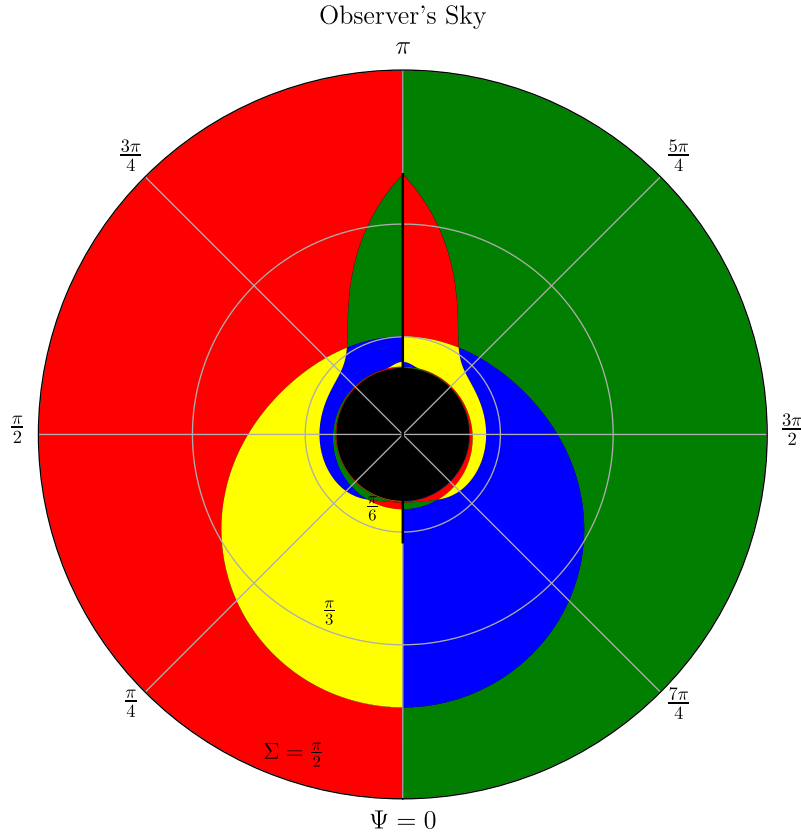


Figure 7. Lens equation of light sources located on the two sphere S_L^2 with radius coordinate $r_L = 9m$ for an observer at $t_O = 0$ located at $r_O = 8m$, $\vartheta_O = \pi/4$ and $\varphi_O = 0$ in the C-metric with $\alpha = 1/(10m)$. The black lines at $\Psi = 0$ and $\Psi = \pi$ indicate light rays crossing the axes at least once.

Bohn et al. [41]. In the following we refer to the area on the sky where $\pi/2 < \Psi < 3\pi/2$ as the northern hemisphere and to the rest of the sky as the southern hemisphere.

Figure 7 shows the lens equation for $\vartheta_O = \pi/4$. There are, for each light source, in principle infinitely many images. We say that an image is of order k if the φ coordinate of the corresponding geodesic ranges over an interval $\Delta\varphi$ with $(k-1)\pi < |\Delta\varphi| < k\pi$. In the centre of the figure we see the shadow. In the outermost part, coloured in red/yellow on the left and in green/blue on the right, there are the primary images ($k = 1$). When we move closer towards the shadow this order reverses and thus these are secondary images, $k = 2$. Moving further in we can also see images of order 3 and 4, where the latter are only visible when zooming into the online version of the figure. The borderlines between images of different orders mark the critical curves. In the Schwarzschild spacetime these are circles (“Einstein rings”). In the C-metric they have a rather complicated shape that varies for the transitions between images of different orders.

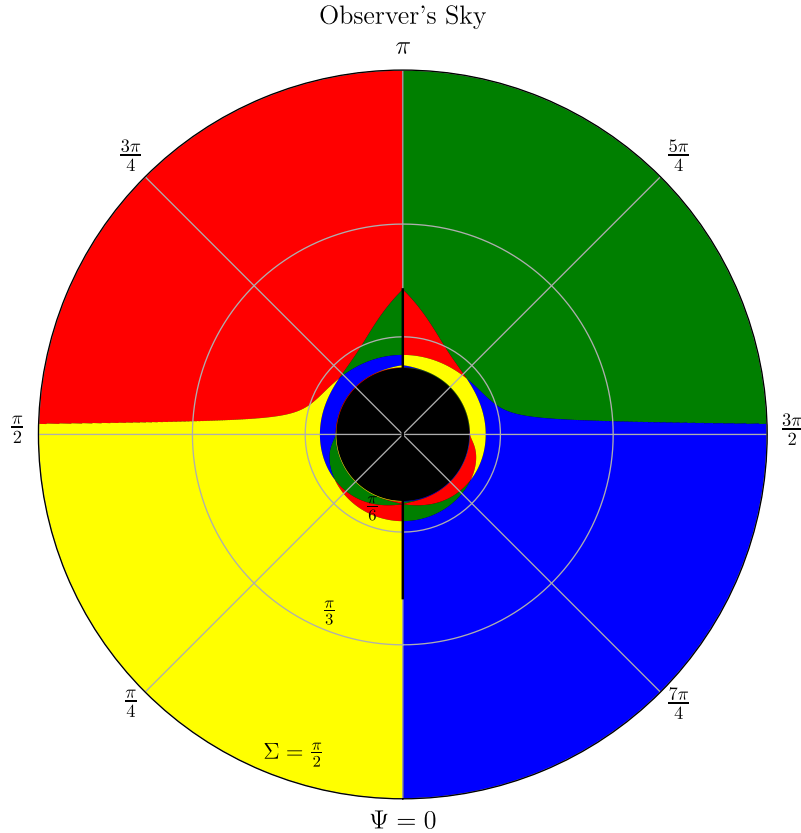


Figure 8. Lens equation of light sources located on the two sphere S_L^2 with radius coordinate $r_L = 9m$ for an observer at $t_O = 0$ located at $r_O = 8m$, $\vartheta_O = \pi/2$ and $\varphi_O = 0$ in the C-metric with $\alpha = 1/(10m)$. The black lines at $\Psi = 0$ and $\Psi = \pi$ indicate light rays crossing the axes at least once.

We also see that on the northern hemisphere images of second and third order can be observed much further away from the shadow than on the southern hemisphere. In particular around $\psi = 0$ higher-order images are visible only very close to the shadow. We also see that light rays travelling towards $\vartheta = 0$ cover the same interval of $\Delta\varphi$ faster than light rays travelling towards $\vartheta = \pi$.

In figure 8 we see the lens map for $\vartheta_O = \pi/2$. This plot clearly demonstrates that in the C-metric there is no symmetry with respect to the plane $\vartheta = \pi/2$. Correspondingly, past-oriented light rays that leave the observer with $|\sin \Psi| = 1$ do *not* necessarily meet the sphere of light sources at $\vartheta_L = \pi/2$. In addition we see that, compared to figure 7, on the northern hemisphere most features, in particular images of second order or higher, are more centred around the shadow while around $\Psi = 0$ they now already appear at a larger distance to the shadow.

In figure 9 we see the lens map for $\vartheta_O = 3\pi/4$. Since the observer is now located at $\vartheta_O > \pi/2$, on the outer part of the image the colours red/yellow and green/blue

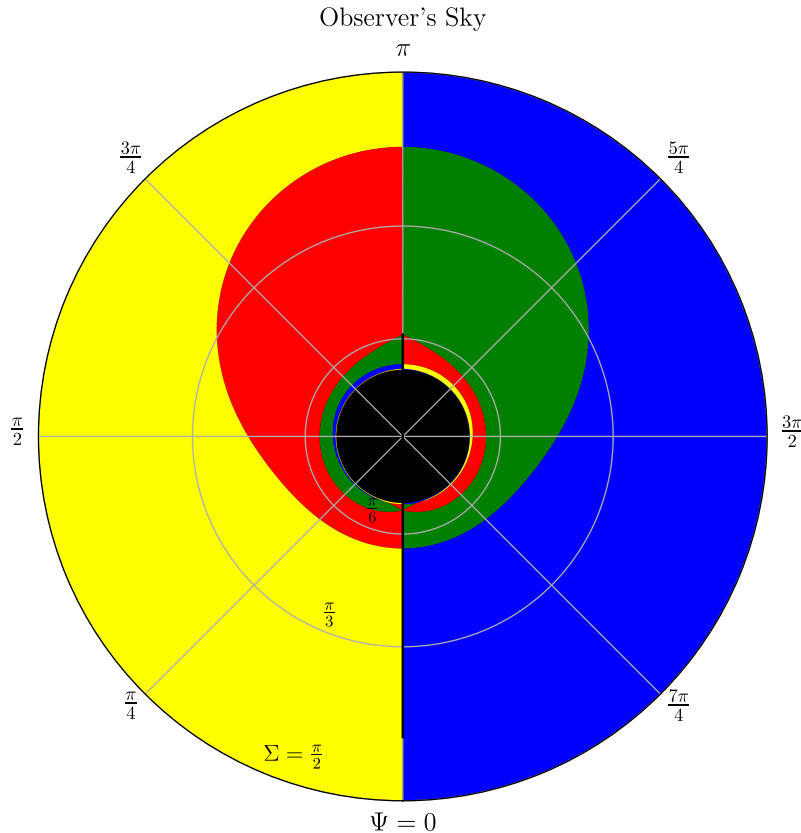


Figure 9. Lens equation of light sources located on the two sphere S_L^2 with radius coordinate $r_L = 9m$ for an observer at $t_O = 0$ located at $r_O = 8m$, $\vartheta_O = 3\pi/4$ and $\varphi_O = 0$ in the C-metric with $\alpha = 1/(10m)$. The black lines at $\Psi = 0$ and $\Psi = \pi$ indicate light rays crossing the axes at least once.

are interchanged with respect to figure 7. On the northern hemisphere images beyond second order can now be observed at angles even closer to the shadow while on the southern hemisphere the images move further away from the shadow.

The broken symmetry with respect to the equatorial plane distinguishes the C-metric from the Schwarzschild metric and from all other spherically symmetric black-hole metrics. In particular, in the C-metric multiple images of a light source are not located on a great circle through the centre of the shadow. This is an observable feature that could become relevant if and when multiple images produced by a black hole are detected.

4.4. Redshift

The redshift is one of the few parameters that are directly accessible to observations. If we can identify emission lines in the spectrum of a light source, we can use them to directly determine the redshift. When we are able to determine the redshift for

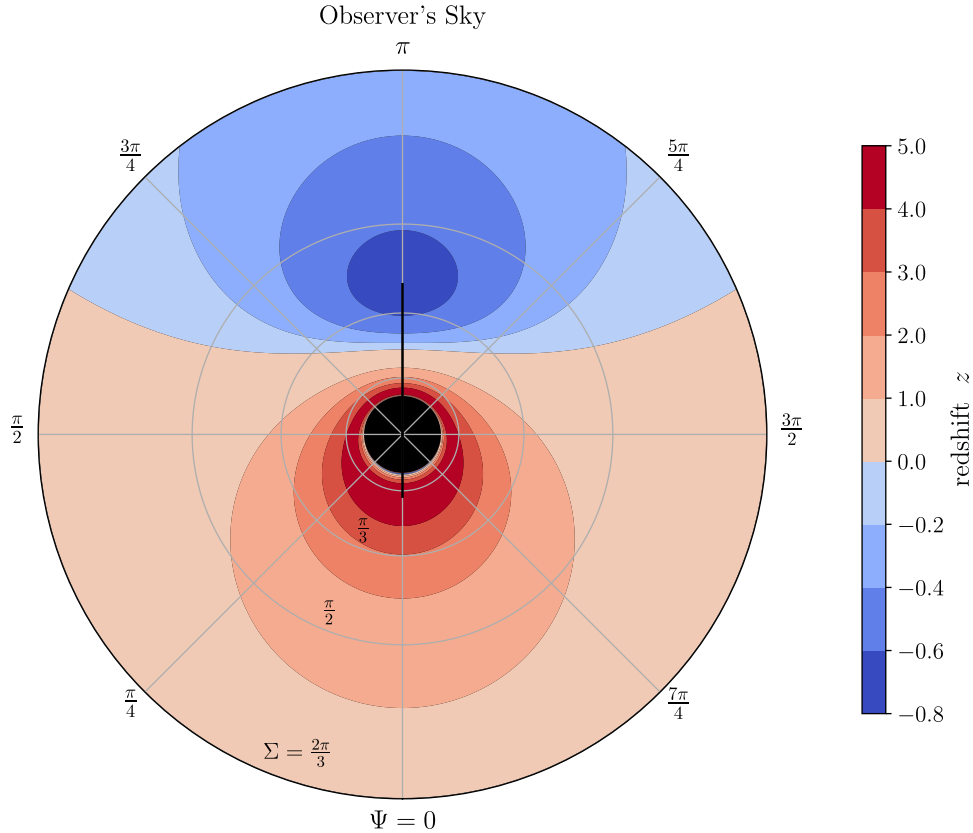


Figure 10. Redshift of light sources located on the two sphere S_L^2 with radius coordinate $r_L = 9m$ measured by an observer at $r_O = 8m$, $\vartheta_O = \pi/4$ in the C-metric with $\alpha = 1/(10m)$. The black lines at $\Psi = 0$ and $\Psi = \pi$ indicate light rays crossing the axes at least once.

sufficiently many pixels in an astrophysical image we can construct a redshift map and draw conclusions on the underlying spacetime by comparing with theoretical predictions.

In the C-metric we consider again, as for the lens map, a static observer at coordinates r_O and ϑ_O and a static light source at coordinates r_L and $\vartheta_L(\Sigma, \Psi)$. The redshift for this situation can be found, e.g., in the book of Straumann [42], pp. 45, and reads

$$z = \sqrt{\frac{g_{tt}|_{x_O}}{g_{tt}|_{x_L}}} - 1. \quad (63)$$

When inserting the g_{tt} of the C-metric this equation becomes:

$$z = \sqrt{\frac{Q(r_O) \Omega(r_L, \vartheta_L(\Sigma, \Psi))}{Q(r_L) \Omega(r_O, \vartheta_O)}} - 1. \quad (64)$$

We can immediately see that, unlike in spherically symmetric and static spacetimes, in the C-metric the redshift does not only depend on the radius coordinates r_O and r_L but

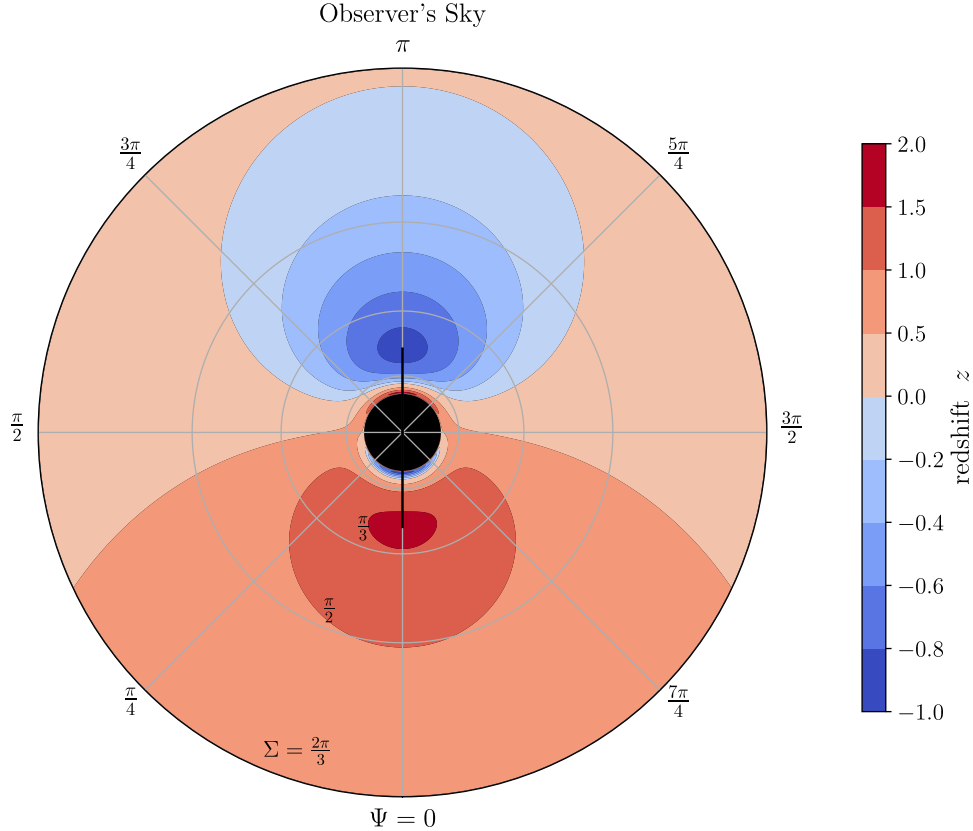


Figure 11. Redshift of light sources located on the two sphere S_L^2 with radius coordinate $r_L = 9m$ measured by an observer at $r_O = 8m$, $\vartheta_O = \pi/2$ in the C-metric with $\alpha = 1/(10m)$. The black lines at $\Psi = 0$ and $\Psi = \pi$ indicate light rays crossing the axes at least once.

also on ϑ_O and $\vartheta_L(\Sigma, \Psi)$ (and via the latter also on the celestial coordinates). Therefore, with r_O , ϑ_O and r_L fixed, the redshift can be considered as a function on the observer's celestial sphere.

Figures 10-12 show the redshift z on the observer's celestial sphere for the same situations as in figures 7-9. Again, we consider the C-metric with $\alpha = 1/(10m)$. For the chosen numbers of $r_O = 8m$ and $r_L = 9m$ the reference redshift (or better blueshift) for the Schwarzschild metric ($\alpha = 0$) is $z = -0.018$.

We can see that in the C-metric the redshift factor varies in the shown images between $z = -1$ and $z = 5$. (From (64) it is clear that z is always bigger than -1.) As for the lens map we can clearly see the axisymmetry of the redshift map. However, the most salient feature is that in contrast to the Schwarzschild metric, where we always observe a blueshift if $r_O < r_L$, for the C-metric we observe both redshifts and blueshifts.

Figure 10 shows the redshift map for an observer at $\vartheta_O = \pi/4$. We can see that the northern hemisphere is dominated by blueshifts and the southern hemisphere is

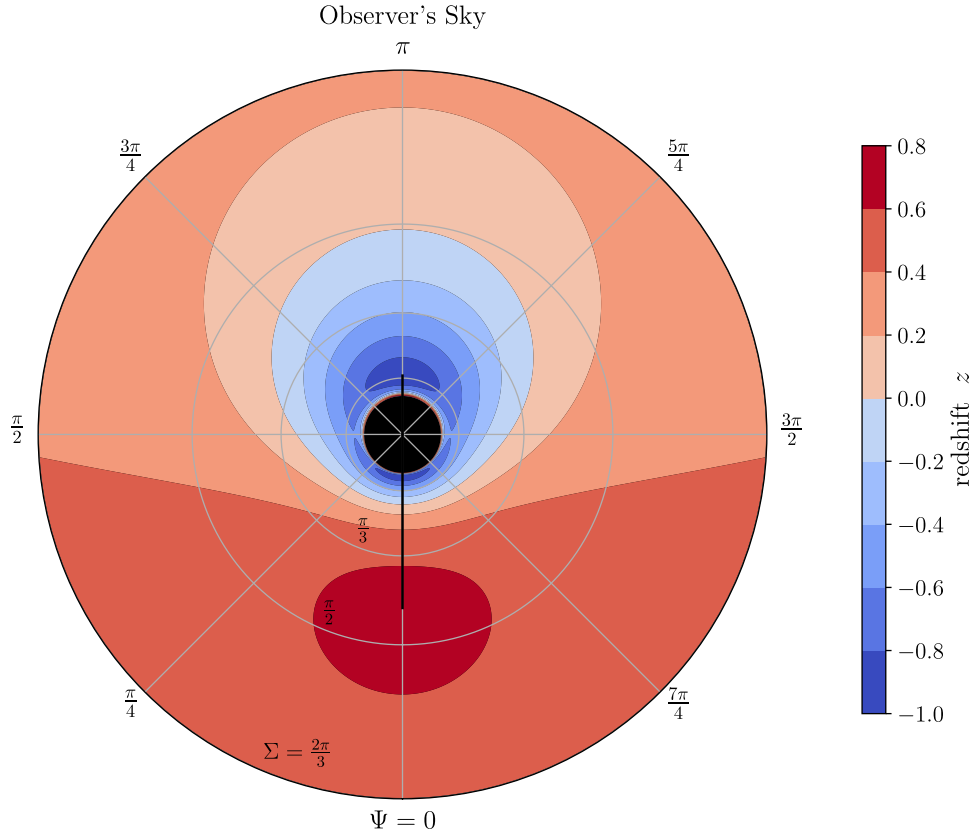


Figure 12. Redshift of light sources located on the two sphere S_L^2 with radius coordinate $r_L = 9m$ measured by an observer at $r_O = 8m$, $\vartheta_O = 3\pi/4$ in the C-metric with $\alpha = 1/(10m)$. The black lines at $\Psi = 0$ and $\Psi = \pi$ indicate light rays crossing the axes at least once.

dominated by redshifts. In addition we can recognise a small and narrow region of blueshifts close to the shadow on the southern hemisphere. (If we zoom in we see a third region of blueshifts even closer to the shadow on the northern hemisphere.) Note that in the redshift equation (64) the root is always constant, so the variation of the redshift factor comes purely from the conformal factor $\Omega(r, \vartheta)$. For $\vartheta_O = \pi/4$ we have $\Omega(r_O, \vartheta_O) < 1$. In addition we have $1/10 \leq \Omega(r_L, \vartheta_L) \leq 19/10$ and in particular $\Omega(r_L, \vartheta_L) < \Omega(r_O, \vartheta_O)$ for $\vartheta_L \leq \vartheta_O$. Thus the closer the light source to the axis $\vartheta = 0$ the higher the blueshift on the northern hemisphere and the closer the light source to the axis $\vartheta = \pi$ the higher the redshift on the southern hemisphere.

Figure 11 shows the redshift map for $\vartheta_O = \pi/2$. As for the lens map we clearly see the asymmetry with respect to the line $|\sin \Psi| = 1$. The range covered by z decreases while the maximum blueshift increases. In addition we observe that on the northern hemisphere the region of blueshift shrinks while it becomes slightly larger on the southern hemisphere. The reduction of the range can be easily understood since in this case we

have $\Omega(r_O, \vartheta_O) = 1$ which is thus larger than for the previous figure.

Figure 12 shows the redshift map for $\vartheta_O = 3\pi/4$. The range of the redshift factor is further reduced since $\Omega(r_O, \vartheta_O) > 1$. The outer part of the figure is now dominated by redshifts. Regions with strong blueshifts now only occur around the shadow and the formerly separated regions in the northern hemisphere and the southern hemisphere connect. Within the region of blueshifts we can still see a small crest-like region of redshifts but it is now much smaller than in the previous figures.

Considering static light sources on a sphere with radius r_L is a convenient way of illustrating the characteristic lensing features in a spacetime. However, light sources which we can actually observe around a black hole are, of course, not located on such a sphere. Therefore, for comparison with observations one has to consider more realistic light sources, e.g. radiating matter that falls towards the black hole or rotates in an accretion disc. It is very well possible to provide redshift maps for such situations in the C-metric but we will not do this here.

4.5. Travel time

The travel time measures, in terms of the time coordinate t , how long a light ray needs to travel along a null geodesic from the light source to the observer. For a light ray emitted by a light source at the time coordinate t_L and detected by an observer at the time coordinate t_O it reads

$$T = t_O - t_L. \quad (65)$$

If an observer sees two images of a light source whose emission varies temporally, then the travel time *difference*, known as the *time delay*, is directly observable. Of course, one has to convert coordinate time into proper time of the observer because only the latter is measurable.

For our specific purposes we set $t_O = 0$. After replacing the integration limits in (47) and substituting for E and K from (58) we obtain the general form of the travel time integral:

$$T(\Sigma) = \int_{r_O \dots}^{\dots r_L} \frac{\sqrt{Q(r_O)} r'^2 dr'}{Q(r') \sqrt{Q(r_O) r'^4 - r_O^2 \sin^2(\Sigma) r'^2 Q(r')}}. \quad (66)$$

It is described in section 3.5 how this travel time integral is to be adapted to each of the different types of r motion.

We see that, if r_O and r_L are fixed, the travel time depends only on the celestial latitude Σ and not on the celestial longitude Ψ . Again, this result is non-trivial because the spacetime is only axisymmetric but not spherically symmetric. Figure 13 shows the travel time for a light ray emitted by a light source located at $r_L = 9m$ and detected by an observer located at $r_O = 8m$ in the C-metric with $\alpha = 1/(10m)$ and, for the sake of comparison, in the Schwarzschild metric ($\alpha = 0$). In either case the travel time diverges if Σ approaches the angular radius of the shadow. The latter is smaller in the C-metric than in the Schwarzschild metric. However, except for Σ close to $\Sigma_{ph,C}$ the travel time

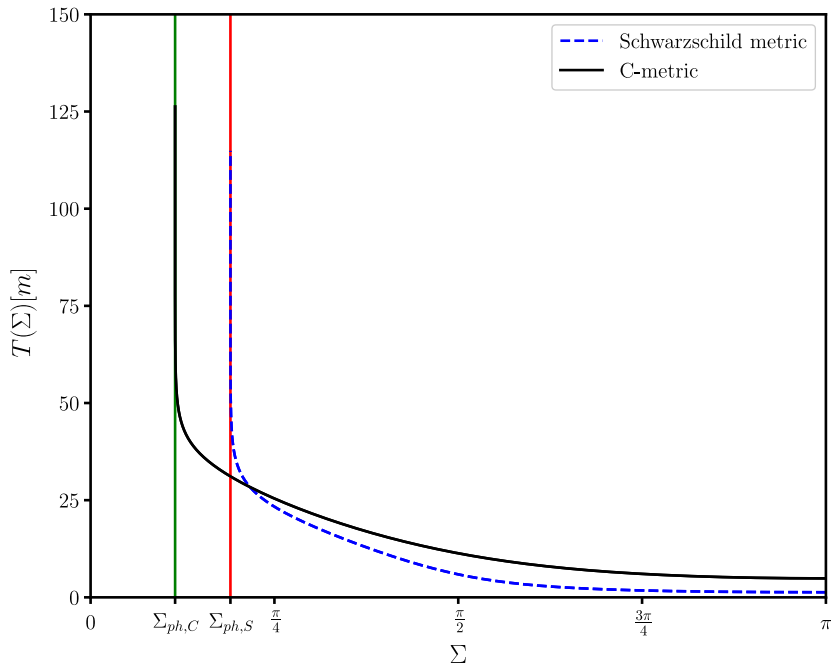


Figure 13. Travel time for a light ray emitted by a light source at $r_L = 9m$ and detected by an observer at $r_O = 8m$ in the Schwarzschild metric (dashed blue line) and in the C-metric with $\alpha = 1/(10m)$ (solid black line). The red and green lines mark the angular radius of the shadow in the Schwarzschild metric $\Sigma_{ph,S}$ and in the C-metric $\Sigma_{ph,C}$, respectively.

of a light ray in the C-metric is longer than for a light ray observed under the same angle Σ in the Schwarzschild metric. Thus one consequence of a non-zero acceleration parameter is an increase of travel time. In addition between $\Sigma = \pi/4$ and $\Sigma = \pi/2$ the travel time increases more slowly for the C-metric than for the Schwarzschild metric.

We have already mentioned that only time delays, i.e., travel time *differences*, in a multiple-imaging situation are observable. This is routinely done for quasars that are multiply imaged by galaxies, see e.g. [43, 44]. Unfortunately, light sources multiply-imaged by black holes have not yet been observed, so we have to wait for future generations of telescopes with higher resolutions before we can confront the results of this section with observations.

5. Conclusions

In the first part of the paper we discussed and solved the equations of motion for lightlike geodesics in the domain of outer communication of the C-metric, using Jacobi's elliptic functions and the elliptic integrals of first and third kind. Whereas in this work we derived the solutions in Boyer-Lindquist-like coordinates, this approach can also be applied to other coordinate systems as, e.g., done very recently in Lim [45] for the

C-metric with a cosmological constant. In particular we derived and discussed the properties of the photon sphere and of the photon cone. It is true that the results on the photon sphere and on the photon cone are not entirely new: The photon sphere was discussed by Grenzebach et al. [18, 19] within a bigger class of spacetimes and by Gibbons and Warnick [21] from a more geometrical point of view; some aspects of the photon cone were presented by Alrais Alawadi et al. [22]. However, we believe that the approach presented here, paralleling the photon sphere and the photon cone by using the potentials V_r and V_ϑ , has some merits and facilitates understanding of the important features.

Based on our representation of the lightlike geodesics in terms of elliptic integrals and elliptic functions, we then gave a detailed account of the lensing features in the C-metric, for static observers and static light sources in the domain of outer communication. More precisely, we calculated the shadow, we worked out a lens equation and we discussed the redshift and the travel time. For achieving these results it was crucial to introduce latitude-longitude coordinates on the observer's celestial sphere which are adapted to an orthonormal tetrad; in this respect our methodology closely followed Grenzebach et al. [18].

In particular, we found that the shadow is circular, for *every* observer in the domain of outer communication. This result is highly non-trivial because the C-metric is not spherically symmetric. We found that the angular radius of the shadow shrinks with increasing acceleration parameter if we keep the radius coordinate r_O of the observer fixed. This result is, however, of limiting usefulness in view of observations as long as we do not know r_O (in units of m) with high accuracy.

As a main result of this paper we derived a lens equation for the C-metric and plotted it on the observer's celestial sphere. We emphasise that our illustrations of this lens equation are based on the analytical solutions of the geodesic equation in terms of elliptic functions and *not* on ray tracing. When zooming into the online version of these illustrations one can identify images up to fourth order. The images also clearly show the critical curves which are the borderlines between images of different orders. In spherical symmetric spacetimes the critical curves are circles ("Einstein rings") but in the C-metric they have a more complicated shape.

For an observer at r_O and light sources at r_L , we calculated and plotted the redshift z as a function on the observer's celestial sphere. In the Schwarzschild metric this function is a constant. (For $r_O < r_L$ it is actually a blueshift.) In the C-metric, however, it is a function of both celestial coordinates, latitude Σ and longitude Ψ . The range of z depends, of course, on the numerical value of the acceleration parameter α and goes to zero for $\alpha \rightarrow 0$. The lowest values of z (in our case blueshifts) occur near the string at $\vartheta = 0$ and the highest values of z (in our case redshifts) occur near the strut at $\vartheta = \pi$.

Lastly we derived the travel time. As in the Schwarzschild spacetime, for an observer at r_O and light sources at r_L the travel time depends only on the celestial latitude Σ . We observed that, keeping r_O , r_L and Σ fixed, the travel time is bigger in the C-metric than in the Schwarzschild metric unless Σ is close to the shadow radius.

In this paper we wanted to provide some theoretical background for distinguishing accelerating black holes from non-accelerating ones by way of lensing observations. It is unfortunate that the *shape* of the shadow is not such a distinguishing feature because the C-metric predicts a circular shadow, just as the Schwarzschild metric. The *size* of the shadow is not a particularly useful observable because it depends not only on the spacetime parameters but also on r_O which is not known with very high accuracy. If we ever see multiple images produced by a black hole, we will be able to determine the parameters of the black hole with much higher accuracy than now: Combining measurements of the redshifts, of the time delay and of the positions in the sky of the images might give us a chance to distinguish accelerating black holes from non-accelerating ones.

Acknowledgment

We acknowledge support from Deutsche Forschungsgemeinschaft within the Research Training Group 1620 Models of Gravity. We also would like to express our gratitude to all contributors to the Julia project and in particular the authors of the packages Elliptic, Blosc, HDF5 and PyPlot. We also would like to thank F. Willenborg for his help with fixing a bug with the layering in the redshift and lens map images.

Appendix A. Integrals for geodesic motion

In this appendix we briefly demonstrate how to calculate the elementary integrals associated with the radius coordinate r and the time coordinate t for lightlike geodesics asymptotically coming from (or going to) the photon sphere and the elliptic integrals associated with t .

Appendix A.1. Elementary integrals

While calculating the solutions for $r(\lambda)$ and $t(\lambda)$ for lightlike geodesics asymptotically coming from (or going to) the photon sphere in Sections 3.2.3 and 3.5.2 we encountered elementary integrals that can be easily solved using coordinate transformations. While in each case the parameters of the integrals vary we can generally transform them into one of the following two forms:

$$I_1 = \int \frac{dy}{(y-a)\sqrt{y-y_1}}, \quad I_2 = \int \frac{dy}{(a-y)\sqrt{y-y_1}}. \quad (\text{A.1})$$

Recall that y_1 is related to the negative root r_4 via (22). Here we have $a = y_{ph}$ in (25) and $I_{ph,4\pm}$ in (50) and $a = \frac{K}{6}$, $a = -\frac{1-6\alpha m}{12}K$ and $a = -\frac{1+6\alpha m}{12}K$ in $I_{ph,1}$, $I_{ph,2}$ and $I_{ph,3}$ in (50), respectively. These integrals can now be solved using simple transformations all containing the constant parameter $a - y_1 > 0$. For $y > a$ we now substitute $z = y - a$ and obtain for I_1 :

$$I_1 = \int \frac{dz}{z\sqrt{z+a-y_1}} = -\frac{2}{\sqrt{a-y_1}} \operatorname{arcoth} \left(\sqrt{\frac{y-y_1}{a-y_1}} \right). \quad (\text{A.2})$$

Analogously for $y < a$ we substitute $z = y - y_1$ and obtain for I_2 :

$$I_2 = \int \frac{dz}{(a - y_1 - z)\sqrt{z}} = \frac{2}{\sqrt{a - y_1}} \operatorname{artanh} \left(\sqrt{\frac{y - y_1}{a - y_1}} \right). \quad (\text{A.3})$$

Now we solve (22) for y and replace all terms containing y , y_{ph} or y_1 in (A.2)-(A.3) to finally obtain the integral on the right-hand side of (25) and $I_{ph,1} - I_{ph,4\pm}$ in (50).

Appendix A.2. Elliptic integrals

An elementary introduction to elliptic integrals and functions can be found in the book of Hancock [34]. In this paper we only need the incomplete elliptic integrals of first and third kind. In Legendre form these integrals read (in order):

$$F_L(\chi, k) = \int_0^\chi \frac{d\chi'}{\sqrt{1 - k \sin^2 \chi'}}, \quad \Pi_L(\chi, k, n) = \int_0^\chi \frac{d\chi'}{(1 - n \sin^2 \chi') \sqrt{1 - k \sin^2 \chi'}}. \quad (\text{A.4})$$

Here, $0 < k < 1$ is the square of the elliptic modulus, $n \in \mathbb{R}$ is an additional parameter and χ is called the amplitude of the elliptic integral.

In addition to the elementary integrals of the previous section in (47), we also encountered one elliptic integral not directly adopting the Legendre form after coordinate transformation (36). In its original form this integral reads:

$$J(\chi_i, \chi, k, n) = \int_{\chi_i}^\chi \frac{d\chi'}{(1 + n \cos \chi') \sqrt{1 - k \sin^2 \chi'}}. \quad (\text{A.5})$$

Now we outline how this integral can be rewritten in terms of the elliptic integrals of first and third kind (A.4). For the calculations we suppress the limits to ease the calculations and to reduce the length of the obtained results.

As a first step we expand by $1 - n \cos \chi$ and split the result into a term containing the elliptic integral of third kind and a second term $L(\chi, k, n)$ only containing an elementary integral:

$$\begin{aligned} J(\chi, k, n) &= \int \frac{d\chi'}{(1 + n \cos \chi') \sqrt{1 - k \sin^2 \chi'}} \\ &= \frac{1}{1 - n^2} \left(\Pi_L \left(\chi, k, \frac{n^2}{n^2 - 1} \right) - nL(\chi, k, n) \right). \end{aligned} \quad (\text{A.6})$$

The computation of $L(\chi, k, n)$ requires several case-by-case analyses and is rather lengthy. Thus we do not reproduce it here and only provide the final result:

$$\begin{aligned} L(\chi, k, n) &= \int \frac{\cos \chi' d\chi'}{\left(1 - \frac{n^2}{n^2 - 1} \sin^2 \chi'\right) \sqrt{1 - k \sin^2 \chi'}} \\ &= \frac{1}{2} \sqrt{\frac{n^2 - 1}{n^2(1 - k) + k}} \ln \left(\frac{\sqrt{\frac{n^2(1-k)+k}{n^2-1}} \sin \chi + \sqrt{1 - k \sin^2 \chi}}{\left| \sqrt{\frac{n^2(1-k)+k}{n^2-1}} \sin \chi - \sqrt{1 - k \sin^2 \chi} \right|} \right). \end{aligned} \quad (\text{A.7})$$

In our case we always integrate over the black hole horizon r_{BH} . Here, $\Pi_L(\chi, k, n^2/(n^2 - 1))$ diverges since we always have $n^2/(n^2 - 1) > 1$. Therefore, we re-arrange the elliptic

integral of third kind in (A.6) such that this divergence vanishes [46]:

$$\begin{aligned} \Pi_L \left(\chi, k, \frac{n^2}{n^2-1} \right) &= F_L(\chi, k) - \Pi_L \left(\chi, k, \frac{k(n^2-1)}{n^2} \right) \\ &+ \frac{1}{2} \sqrt{\frac{n^2(n^2-1)}{n^2(1-k)+k}} \ln \left(\frac{\cos \chi \sqrt{1-k \sin^2 \chi} + \sqrt{\frac{n^2(1-k)+k}{n^2(n^2-1)}} \sin \chi}{\left| \cos \chi \sqrt{1-k \sin^2 \chi} - \sqrt{\frac{n^2(1-k)+k}{n^2(n^2-1)}} \sin \chi \right|} \right). \end{aligned} \quad (\text{A.8})$$

Appendix B. Solving differential equations using Jacobi's elliptic functions

Using a suitable coordinate transformation every equation of the form (9) or (10) can be transformed into the Legendre form

$$\left(\frac{d\chi}{d\lambda} \right)^2 = a(1 - k \sin^2 \chi), \quad (\text{B.1})$$

where for the time being λ shall be an arbitrary real parameter and the constant a always depends on the coefficient of the highest order. Since we only look for physical solutions we deal with real quantities and thus in our case this constant turns out to always be real and positive. Therefore, in the following we restrict our discussion to this scenario.

Let us now assume that we have a physical setting with initial condition $\chi(\lambda_i) = \chi_i$ and let us denote the sign of the motion by $i_{\chi_i} = \text{sign}(d\chi/d\lambda|_{\lambda_i})$. In a first step we separate variables and we integrate using the given initial conditions:

$$\lambda - \lambda_i = \int_{\lambda_i}^{\lambda} d\lambda' = i_{\chi_i} \int_{\chi_i}^{\chi} \frac{d\chi'}{\sqrt{a(1 - k \sin^2 \chi')}}. \quad (\text{B.2})$$

Now we move all terms containing the parameter or information on the initial condition to the left-hand side:

$$\tilde{\lambda}(\lambda) = i_{\chi_i} \sqrt{a}(\lambda - \lambda_i) + \int_0^{\chi_i} \frac{d\chi'}{\sqrt{1 - k \sin^2 \chi'}} = \int_0^{\chi} \frac{d\chi'}{\sqrt{1 - k \sin^2 \chi'}}. \quad (\text{B.3})$$

Using the relation between amplitude χ and $\tilde{\lambda}$, $\chi = \text{am}(\tilde{\lambda})$, we see that (B.1) is solved by the Jacobian elliptic sn function:

$$\sin \chi(\lambda) = \text{sn}(\tilde{\lambda}(\lambda), k) = \text{sn}(i_{\chi_i} \sqrt{a}(\lambda - \lambda_i) + \lambda_{\chi_i, k}, k), \quad (\text{B.4})$$

where we defined a new quantity $\lambda_{\chi_i, k}$ that depends on the initial condition. Analogously for an appropriate coordinate transformation containing $\cos \chi$ we have $\cos \chi(\lambda) = \cos \text{am}(\tilde{\lambda}(\lambda)) = \text{cn}(\tilde{\lambda}(\lambda), k)$ and thus in these cases we can write the solution of the general equation in terms of

$$\cos \chi(\lambda) = \text{cn}(\tilde{\lambda}(\lambda), k) = \text{cn}(i_{\chi_i} \sqrt{a}(\lambda - \lambda_i) + \lambda_{\chi_i, k}, k). \quad (\text{B.5})$$

References

- [1] The Event Horizon Telescope Collaboration 2019 *Astrophys. J. Lett.* **875**(1) L1
- [2] Kardashev N S *et al.* 2013 *Astron. Rep.* **57**(3) 153–194

- [3] Kardashev N S *et al.* 2017 *Sol. Syst. Res.* **51**(7) 535–554
- [4] Levi-Civita T 1918 *Rend. Accad. Lincei* **27**(2) 343–351
- [5] Plebanski J F and Demianski M 1976 *Ann. Phys. (N. Y.)* **98**(1) 98–127
- [6] Ehlers J and Kundt W 1962 Exact solutions of the gravitational field equations *Gravitation: An Introduction to Current Research* ed Witten L (Wiley: New York) pp 49–101
- [7] Griffiths J B, Krtouš P and Podolský J 2006 *Class. Quantum Grav.* **23**(23) 6745–6766
- [8] Griffiths J B and Podolský J 2009 *Exact Space-Times in Einstein's General Relativity* (Cambridge: Cambridge University Press) ISBN 978-0-521-88927-8
- [9] Aichelburg P C and Sexl R U 1971 *Gen. Relativ. Gravit.* **2**(4) 303–312
- [10] Kinnersley W and Walker M 1970 *Phys. Rev. D* **2**(8) 1359–1370
- [11] Kofroň D 2020 *Gen. Relativ. Gravit.* **52**(9) 91
- [12] Farhoosh H and Zimmerman L 1980 *Phys. Rev. D* **21**(2) 317–327
- [13] Pravda V and Pravdová A 2001 *Class. Quantum Grav.* **18**(7) 1205–1216
- [14] Chamblin A 2001 *Class. Quantum Grav.* **18**(3) L17–L22
- [15] Podolský J, Ortogio M and Krtouš P 2003 *Phys. Rev. D* **68**(12) 124004
- [16] Bini D, Cherubini C, Gerialico A and Mashhoon B 2005 *Class. Quantum Grav.* **22**(4) 709–722
- [17] Lim Y K 2014 *Phys. Rev. D* **89**(10) 104016
- [18] Grenzebach A, Perlick V and Lämmerzahl C 2015 *Int. J. of Mod. Phys. D* **24**(9) 1542024
- [19] Grenzebach A 2016 *The Shadow of Black Holes* Springer Briefs in Physics (Heidelberg: Springer)
- [20] Hong K and Teo E 2003 *Class. Quantum Grav.* **20**(14) 3269–3277
- [21] Gibbons G W and Warnick C M 2016 *Phys. Lett. B* **763** 169–173
- [22] Alrais Alawadi M, Batic D and Nowakowski M 2021 *Class. Quantum Grav.* **38**(4) 045003
- [23] Yang X and Wang J 2013 *Astrophys. J. Suppl. Ser.* **207**(1) 6
- [24] Forsyth A R 1920 *Proc. Math. Phys. Eng. Sci.* **97**(682) 145–151
- [25] Morton W B 1921 *Lond. Edinb. Dubl. Phil. Mag.* **42**(250) 511–522
- [26] Darwin C 1959 *Proc. R. Soc. Lond. A, Math. Phys. Sci.* **249**(1257) 180–194 URL <https://www.jstor.org/stable/100508>
- [27] Gralla S E and Lupsasca A 2020 *Phys. Rev. D* **101**(4) 044032
- [28] Sharif M and Iftikhar S 2016 *Astrophys. Space Sci.* **361**(1) 36
- [29] Clément G, Gal'tsov D and Guenouche M 2015 *Phys. Lett. B* **750** 591–594
- [30] Griffiths J B and Podolský J 2005 *Class. Quantum Grav.* **22**(17) 3467–3479
- [31] Chng B, Mann R and Stelea C 2006 *Phys. Rev. D* **74**(8) 084031
- [32] Podolský J and Vrátný A 2020 *Phys. Rev. D* **102**(8) 084024
- [33] Mino Y 2003 *Phys. Rev. D* **67**(8) 084027
- [34] Hancock H 1917 *Elliptic Integrals* 1st ed Mathematical Monographs (New York John Wiley & Sons)
- [35] Bezanson J, Edelman A, Karpinski S and Shah V B 2017 *SIAM Rev.* **59**(1) 65–98
- [36] Synge J L 1966 *Mon. Not. R. Astron. Soc.* **131**(3) 463–466
- [37] Grenzebach A, Perlick V and Lämmerzahl C 2014 *Phys. Rev. D* **89**(12) 124004
- [38] Grenzebach A 2015 Aberrational Effects for Shadows of Black Holes *Equations of Motion in Relativistic Gravity* ed Puetzfeld D, Lämmerzahl C and Schutz B (Cham: Springer)
- [39] Frittelli S and Newman E T 1999 *Phys. Rev. D* **59**(12) 124001
- [40] Perlick V 2004 *Phys. Rev. D* **69**(6) 064017
- [41] Bohn A, Throwe W, Hébert F, Henriksson K, Bunandar D, Scheel M A and Taylor N W 2015 *Class. Quantum Grav.* **32**(6) 065002
- [42] Straumann N 2013 *General Relativity* 2nd ed Graduate Texts in Physics (Heidelberg: Springer) ISBN 978-94-007-5409-6
- [43] Koptelova E, Chen W P, Chiueh T, Artamonov B P, Oknyanskij V L, Nuritdinov S N, Burkhanov O, Akhunov T, Bruevich V V, Ezhkova O V, Gusev A S, Sergeev A V, Ehgamberdiev S A and Ibragimov M A 2012 *Astron. Astrophys.* **544** A51
- [44] Fohlmeister J, Kochanek C S, Falco E E, Wambsganss J, Oguri M and Dai X 2013 *Astrophys. J.*

764(2) 186

- [45] Lim Y K 2021 *Phys. Rev. D* **103**(2) 024007
- [46] Milne-Thomson L M 1972 Elliptic Integrals *Handbook of Mathematical Functions With Formulas, Graphs, and Mathematical Tables* Applied Mathematics Series ed Abramowitz M and Stegun I A (Washington D. C.: U. S. Dept. of Commerce, National Bureau of Standards) pp 587–607
10th ed